Super-resolution imaging pinpoints ultrastructural changes at the node of Ranvier in patients with polyneuropathy

Luise Appeltshauser[1 *], Janis Linke[1,2 *], Hannah S. Heil[2,3 *], Christine Karus[2], Joachim Schenk[2], Katherina Hemmen[2], Claudia Sommer[1], Kathrin Doppler[1] ✉, and Katrin G. Heinze[2] ✉

[1]Department of Neurology, University Hospital Würzburg, Würzburg, Germany
[2]Rudolf Virchow Center, Center for Integrative and Translational Bioimaging, University of Würzburg, Würzburg, Germany
[3]Current affiliation: Optical Cell Biology, Instituto Gulbenkian de Ciência, Oeiras, Portugal
[*]these authors are co-first authors

The peripheral node of Ranvier is the key element in saltatory conduction along myelinated axons, but its ultrastructural protein arrangement and interactions remain elusive in humans. To assess both physiological protein arrangement and pathological ultrastructural changes at the paranodal region of the node of Ranvier, we implement the super resolution microscopy method "*direct* Stochastic Optical Reconstruction Microscopy" (*d*STORM) assisted by high-content confocal microscopy on nerve biopsies of patients with polyneuropathies. We demonstrate that a ∼190nm periodic arrangement of axonal cytoskeletal proteins is conserved in humans, but impaired at the paranode in polyneuropathy. In patients with polyneuropathy, the periodic protein distances of the paranodal adhesion molecules Caspr-1 and neurofascin-155 were severely elongated, implying a lateral decoiling and partial loss of the axoglial complex at the node of Ranvier. Dual-color colocalization analysis of the super-resolved *d*STORM images revealed that the axoglial complex itself remained closely attached even under pathological conditions, but was detached from its cytoskeletal axonal anchor. Correspondingly, high-content confocal analysis of nodes of Ranvier showed that paranodal elongation occurred especially in acute and severe axonal neuropathy. Our findings show that super-resolution techniques open the possibility to identify underlying nanoscale pathology in polyneuropathies, with possible future use in diagnostic assessment.

Super-resolution Microscopy | Polyneuropathy | Node of Ranvier

Correspondence:
Doppler_K@ukw.de & katrin.heinze@virchow.uni-wuerzburg.de

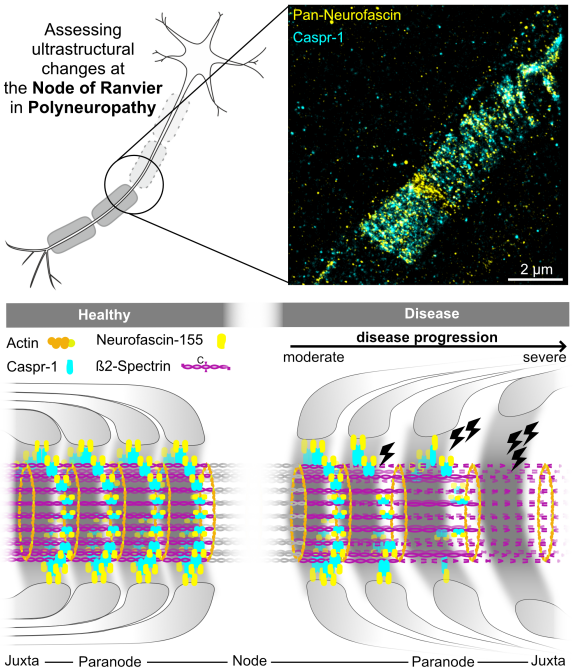

Graphical abstract: Mapping the ultrastructural organization of axoglial proteins at the node of Ranvier in nerve fibers by *d*STORM microscopy in health and disease. Super-resolution microscopy reveals the 190 nm periodic arrangement of structural proteins (axonal ß2-spectrin, Caspr-1 and neurofascin-155) in the healthy node of Ranvier in teased fiber preparations becoming severely disrupted in polyneuropathy patients where a loss of Caspr-1 and neurofascin-155 weakens attachment of the myelin loops. These fine periodic structures would remain hidden in conventional fluorescence microscopy. Scale bar 2 µm.

Introduction

The node of Ranvier of myelinated axons is the key element for rapid long-distance neuronal signal transduction via saltatory conduction (1, 2). Saltatory conduction requires a highly specialized Schwann cell- axon interplay at the node of Ranvier (3, 4): The highly organized nanostructure of the node of Ranvier allows to cluster ion channels at the nodal region and to secure cell adhesion at the paranodal and juxtaparanodal region (5–7). Selected cell adhesion proteins at the paranode are glial neurofascin-155 and axonal contactin-1 associated protein 1 (Caspr-1). They form part of the axoglial complex and attach the terminal myelin loops to the axon, thus contributing to the maintenance of the nodo-paranodal ultrastructure and fast propagation of action potentials (2, 8–11). In polyneuropathy, the most common disorder of the peripheral nervous system (12), fast signal transduction is impaired. Different pathomechanisms lead to axonal, myelin and Schwann cell damage, resulting in severe sensorimotor deficits with disability in affected patients (12, 13). In recent years, the essential role of the node of Ranvier and the severe consequences of its alterations have been studied in acquired and hereditary neuropathies, particularly in autoantibody-mediated inflammatory neuropathies (14–18). Yet, little is known about the ultrastructural arrangement of the node of Ranvier in polyneuropathies of other etiologies. New means to assess ultrastructural pathologic changes could therefore help to unravel distinct pathomechanisms and en-

hance the diagnostic work-up of polyneuropathies.

In rodents, new super-resolution imaging techniques like stimulated emission depletion (STED) (19) have shed light on the ultrastructural arrangement of the node of Ranvier: Ion channels, axonal scaffold proteins and cell adhesion molecules of the axoglial junction are arranged following a 190 nm periodicity (20). This periodic arrangement has earlier been demonstrated in axonal scaffold proteins throughout the axon and is well conserved across species (21–24).

Resolving such small protein periodicities would not be possible without the application of super-resolution microscopy. New techniques provide an unpreceded insight into the molecular organization and protein interaction in the context of health and disease (25). STED and (direct) Stochastic Optical Reconstruction Microscopy ((*d*)STORM) combine target specificity with a very high spatial resolution (26, 27) and allow analysis of periodic ultrastructures by computational autocorrelation analysis of the images (20, 23, 24, 27, 28). In contrast to STED, Single Molecule Localization Microscopy (SMLM) in general and *d*STORM in particular pinpoint molecular positions in cells and tissue with nanometer precision. With hundreds and thousands of hits per image, *d*STORM provides maps of the subcelllar architecture as a prerequisite for further analysis of molecular clusters, colocalization and relative position distributions in higher order structures (29–31). So far, STED and SMLM have mainly been applied to map the neuronal nanoscale anatomy under physiological(20, 23, 24, 32, 33), but rarely under pathological conditions (34, 35).

Here, we study the node of Ranvier by *d*STORM and complementary modalities, especially in human samples, which has not been addressed so far despite its potential for new insights into ultrastructural changes on a nanoscale level in the context of polyneuropathies. Thereby, we shed light on distinct pathomechanisms with direct implications for diagnosis and treatment. We use the super-resolved *d*STORM images on ex vivo human sensory nerve teased fiber preparations of patients with polyneuropathy to analyze the nanoscale periodicity of selected adhesion and scaffold proteins at the node of Ranvier. To reveal underlying mechanisms of pathological alterations, we assessed the interaction of the axoglial adhesion molecules neurofascin-155 and Caspr-1 and the axonal scaffold protein ß2-spectrin including dual-color colocalization analysis. The development of a tailored high-content confocal imaging pipeline allowed us to assess node of Ranvier morphometrics in polyneuropathies. Considering histopathological acuteness, type and severity of the disease as well as clinical features in the analysis, we could relate our nanoscale findings to histopathological and clinical data.

Results

Definition and validation of histopathological categories of polyneuropathy. In order to assess the nodo-paranodal nanoscale organization in the human species and to identify possible pathological changes, we included n = 17 patients with polyneuropathy into our study. These had undergone sensory nerve biopsy (n = 16 sural nerve, n = 1 radial superficial nerve) during the routine diagnostic workup process of polyneuropathy. Demographic data and electrophysiological and clinical diagnosis including diagnostic criteria are listed in Supplemental Table S1. Histopathological diagnosis was assessed from semithin cross sections stained with toluidine blue and immunostainings and evaluated by an experienced examiner. Type (axonal/demyelinating), acuteness (acute/chronic) and severity of axonal loss (mild/moderate/severe) were rated in each individual (see Supplemental Table S2). Histopathological parameters differed significantly in acute vs. chronic and axonal vs. demyelinating neuropathy. Furthermore, clinical disease duration significantly differed in histopathologically acute vs. chronic neuropathy (see Supplemental Table S3 and Supplemental Figure S1). According to this rating, we sperated our patients into three histopathological subcohorts: acute axonal neuropathy (n = 6 patients), chronic axonal neuropathy (n = 6 patients) and chronic demyelinating neuropathy (n = 5 patients). Furthermore, we assessed the severity of axonal loss measuring the cross-sectional density of myelinated fibers. The number of fibers per mm^2 was significantly reduced in acute vs. chronic neuropathy. The amplitude of the sensory nerve action potential correlated to the number of fibers per mm^2 and was significantly reduced in severe vs. mild disease (see Supplemental Table S3 and Supplemental Figure S1). Thus, histopathological categories were validated clinically and electrophysiologically, allowing a direct comparison of ultrastructural changes in nodo-paranodal nanoscale organization in relation to type, acuteness and severity of neuropathy.

Development and validation of a *d*STORM autocorrelation analysis tool. To analyze the periodic arrangement of structural proteins in the internodal and paranodal region in ex vivo tissue samples with *d*STORM microscopy, we developed a custom image analysis tool implemented in MatLab (Mathworks Inc.). The general image processing workflow is illustrated in Supplemental Figure S2. As patient derived tissue preparations pose a whole set of challenges when it comes to sample preparation for super-resolution imaging, especially concerning immunolabeling efficiency and non-specific binding, we validated our image based autocorrelation analysis using simulated datasets. To define a ground truth model for our simulations, we assumed a 190 nm periodic arrangement of paranodal proteins, as previously described using STED in rodent teased fiber preparations (20). Then, we tested whether the autocorrelation script for analysis was suitable concerning high level of accuracy and robustness. As a result, we could reliably detect this 190 nm periodic arrangement even in conditions with high background levels and strongly reduced marker densities (Figure 1, A-E).

The adult human axonal internodal scaffold follows a 190 nm periodic arrangement. We then implemented the autocorrelation analysis on super-resolved *d*STORM image reconstructions of murine and human teased fiber preparations. First, we assessed cytoskeletal protein periodicities in the internodal segment by analysis of ß2-spectrin. By apply-

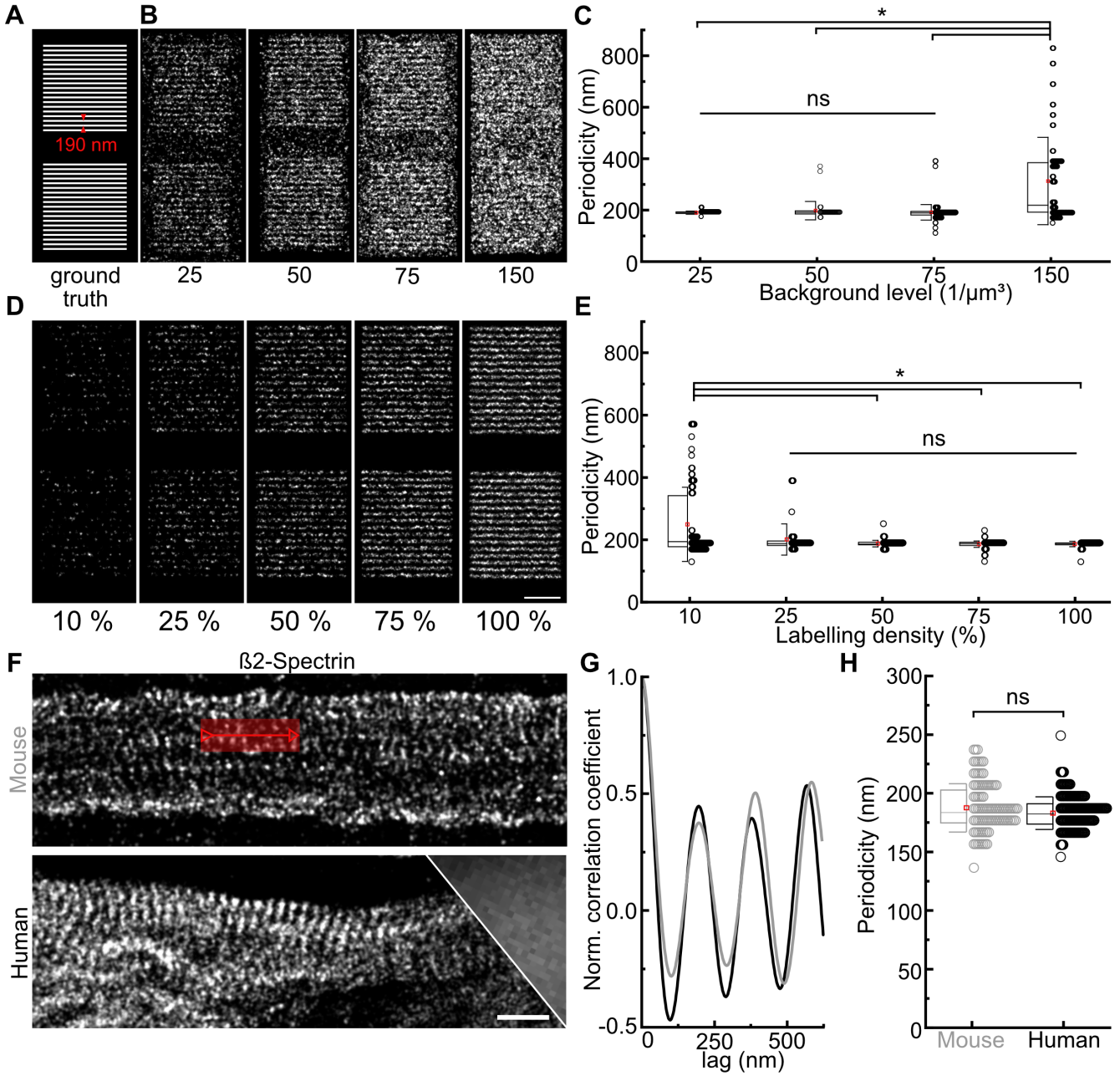

Fig. 1. *d*STORM image autocorrelation analysis is robust to labeling artifacts and resolves the periodic cytoskeletal ultrastructure at the internode in rodents and humans. (A) The robustness of image autocorrelation analysis is tested on simulated Single Molecule Localisation Microscopy (SMLM) data based on a line structure with 190 nm periodicity as ground truth. (B) For background levels ranging from 25 - 150 events/µm^3, autocorrelation recovers the underlying periodicity spacing as visualized in (C) boxplots , only failing at the highest background level (median ± standard deviation; 25: 190 ± 6 nm, n = 99; 50: 190 ± 36, n = 90; 75: 188 ± 30 nm, n = 143; 150: 218 ± 170 nm, n = 88; Kruskal-Wallis test). (D) Using labeling densities from 10 to 100%, autocorrelation (E) successfully retrieves the periodicity spacing at minimum 25% (median ± standard deviation; 10%:194 ± 119 nm, n = 91; 25%: 188 ± 50 nm, n = 94; 50%: 186 ± 11 nm, n = 131; 75%: 188 ± 11 nm, n = 150; 100%: 188 ± 9 nm, n = 134; Kruskal-Wallis test). (F) SMLM resolves the longitudinal periodic arrangement (red arrow) of internodal ß2-spectrin in teased fiber preparations of murine (top) and human (bottom) axons, in contrast to conventional diffraction-limited widefield microscopy (inset, right). (G) Oscillating normalized correlation coefficient curves show equal 190 nm peak-to peak distances and thus an equal periodic arrangement of murine (gray) and human (black) axonal ß2-spectrin. (H) Boxplots of the distribution of periodic spacings measured by the autocorrelation analysis in murine (n = 99) and human teased fiber preparations (n = 192) show no significant differences in median periodic arrangement between the two species, tested by Mann-Whitney test. Boxplots display mean (red square), median (line), standard deviation (whiskers) and 25-75% (box). Scale bars 1 µm.

ing *d*STORM microscopy, we could increase the resolution in comparison to diffraction-limited microscopy, which allowed us to display periodic arrangement of internodal ß2-spectrin as shown in Figure1F. Autocorrelation analysis revealed a mean periodicity of 188 nm in mice, thus corresponding to previously described data on the periodic arrangement of axonal structural proteins (see above). In adult human sural nerve ex vivo teased fibers preparations, we found a mean periodicity of 184 nm. This leads us to the conclusion that the ∼190 nm structural protein periodicity is conserved in human adults, without any significant difference compared to rodents (see Figure 1, G-H; detailed values including standard deviation and p-values are shown in Supplemental Table S4).

Disruption of the ultrastructural periodic arrangements of paranodal proteins in patients with polyneuropathies. We then addressed the ultrastructural protein arrangement in the paranodal region of the node of Ranvier in rodents and humans. First, we analyzed the periodicity of axonal cytoskeletal ß2-spectrin in the paranodal compartment. In contrast to the internodal segment, the ultrastructural arrangement of ß2-spectrin was altered at the paranodal axon in patients with axonal neuropathies (see Figure 2, A, C, E). We could detect a significant increase of the periodicity of ß2-spectrin at the paranode in patients with axonal neuropathies compared to rodents (202 vs 184 nm, $p = 0.002$). In patients with demyelinating neuropathies, however, the paranodal ß2-spectrin periodicity did not differ significantly from rodents (191 vs 184 nm, $p = 0.78$). Differences in periodicity between patients with axonal and demyelinating disease were not significant. Detailed values including standard deviations are shown in Supplemental Table S4. Next, we assessed the paranodal axoglial junctional protein Caspr-1, located at the axon together with contactin-1 and tethered to axonal ß2-spectrin through protein 4.1B, and their glial binding partner neurofascin-155 (6, 8, 36, 37). The mean periodic distance of the axonal cell adhesion molecule Caspr-1 was severely elongated in patients with axonal and demyelinating neuropathy compared to rodents (247 ± 99 nm vs 187 ± 25 nm, $p < 0.0001$, see Figure 2, B, D and F and Supplemental Table S4). The same applied for its glial counterpart neurofascin-155 (284 ± 125 nm vs 173 ± 24 nm, $p < 0.0001$, see Figure 2F and Supplemental Table S4). As expected, we observed a broad distribution of spacings in humans that ranged from "healthy" nodes (with maintained physiological periodic arrangement) to highly pathological nodes (with disturbed periodicity). Selected nodes of Ranvier even showed unilateral paranodal pathology only: Figure 2D illustrates that pathological alterations of the paranodal nanostructure follow a longitudinal direction, with a mid-to-lateral increase in periodic protein distance. The mid-to-lateral increase in periodicity thus resembles a loosening of the Caspr-1 helical arrangement with lateral diffusion in pathologically altered nodes of Ranvier.

In conclusion, *d*STORM was able to detect pathological alterations of the paranodal periodic protein arrangement in polyneuropathy in general, but especially on the level of individual nodes and patients, thus demonstrating its potential aptitude to assess nanoscale pathology in individuals.

Paranodal neurofascin and Caspr-1 closely attach even in pathologically altered nerves. We performed a colocalization analysis of Caspr-1, neurofascin-155 and ß2-spectrin on drift-corrected dual-color *d*STORM datasets of murine and human teased nerve fibers. To quantitatively assess colocalization, we calculated and compared Manders' A and B coefficients of colocalization (38, 39). In murine samples, we could confirm a high level of colocalization of the components of the axoglial junction, Caspr-1 and glial neurofascin-155, represented by high Manders' coefficients. Furthermore, we observed a colocalization of Caspr-1 with its axonal anchor molecule ß2-spectrin (Figure 3, A-B and Supplemental Table S4). In human samples of patients with both axonal and demyelinating polyneuropathies, our data indicated an integrity of the paranodal axoglial complex of Caspr-1 and neurofascin-155, even if nodo-paranodal architecture was severely disrupted: Although super-resolution images showed a disruption of the paranodal architecture with partial loss of the axoglial complex in patients with polyneuropathies (see Figure 3C), Manders' A and B correlation coefficients did not decrease compared to murine samples in patients with demyelinating, chronic axonal and acute axonal neuropathies (see Figure 3E and Supplemental Table S4). However, the colocalization of axonal Caspr-1 with the paranodal fraction of cytoskeletal ß2-spectrin was disrupted in patients with both axonal and demyelinating polyneuropathies: Manders' A and B correlation coefficients were significantly reduced compared to murine samples, with the strongest effect in patients with acute axonal polyneuropathy (see Figure 3, D and F and Supplemental Table S4). In some areas of the paranode where ß2-spectrin periodicity was increased, Caspr-1 staining was lost completely (see Figure 3D). In conclusion, our data indicate that axoskeletal alterations could contribute to lateral diffusion and loss of the axoglial complex at the paranodes, as the junctional complex itself remains closely attached even in pathologically altered nodes.

High-content confocal imaging of nerve teased fiber preparations reveals nodo-paranodal damage in patients with axonal polyneuropathies. To relate our findings on a nanoscale level to the analysis of a higher number of nodes per patient, to "capture the bigger picture" of node of Ranvier pathology in patients with polyneuropathies of different etiologies and to evaluate its diagnostic potential, we performed high-content confocal imaging including large field of view photomicrographs on teased fiber preparations that had undergone triple immunostaining including myelin markers (myelin basic protein, MBP) and nodo-paranodal markers (Caspr-1, Pan-Neurofascin, see Figure 4A). We combined automated and manual image analysis to assess the number of nodes of Ranvier and node of Ranvier morphometrics (see Figure 4B) to obtain physiological and pathological nodo-paranodal parameters and evaluated differences in different types and stages of neuropathy.

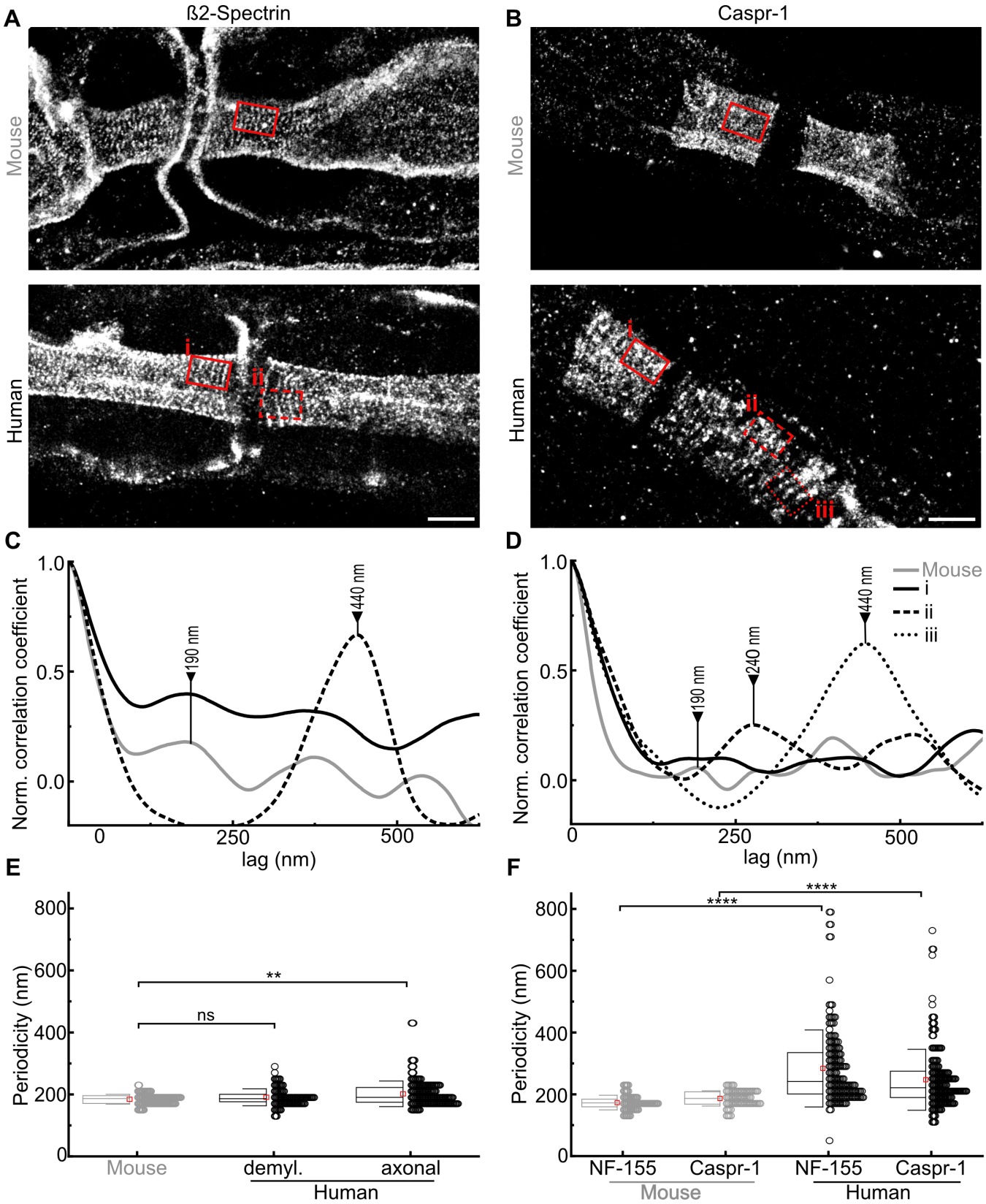

Fig. 2. Periodic spacings of cytoskeletal proteins and axoglial adhesion proteins are increased in patients with polyneuropathies. (A-B) Super-resolved image reconstruction of (A) cytoskeletal ß2-spectrin and (B) axonal adhesional Caspr-1 organization at the node of Ranvier in teased fiber preparations of murine (top) and human (bottom) ex vivo axons. (C-D) Autocorrelation coefficient curves of the image regions marked in red in (A-B) of the distribution of ß2-spectrin (C) and Caspr-1 (D) in murine (gray lines) and human (black lines) teased fiber preparations indicating a local extension of the observed periodicity in pathological affected paranodes (dashed and dotted lines). (E) Boxplots of the distribution of periodic spacings of paranodal ß2-spectrin measured by autocorrelation analysis in mice (n = 130) and patients with histopathologically demyelinating (demyl., n = 106) and axonal (n = 159) neuropathy show a significant increase in cytoskeletal ß2-spectrin periodic arrangement in patients with axonal neuropathy, but not with demyelinating neuropathy. (F) Boxplots of the distribution of periodic spacings of Caspr-1 and neurofascin-155 (NF-155) in mice (n = 80 & 92) and in patients (n=194 & 173) show a highly significant increase in periodic spacings of axoglial proteins in patients with all types of polyneuropathies, with high variance between single regions of interest. Kruskal-Wallis test with Dunn's correction for multiple testing was used for comparison. Significance level: * $p < 0.05$, ** $p < 0.01$, *** $p < 0.001$, **** $p < 0.0001$. Boxplots display mean (red square), median (line), standard deviation (whiskers) and 25-75% (box). Scale bars 2 µm.

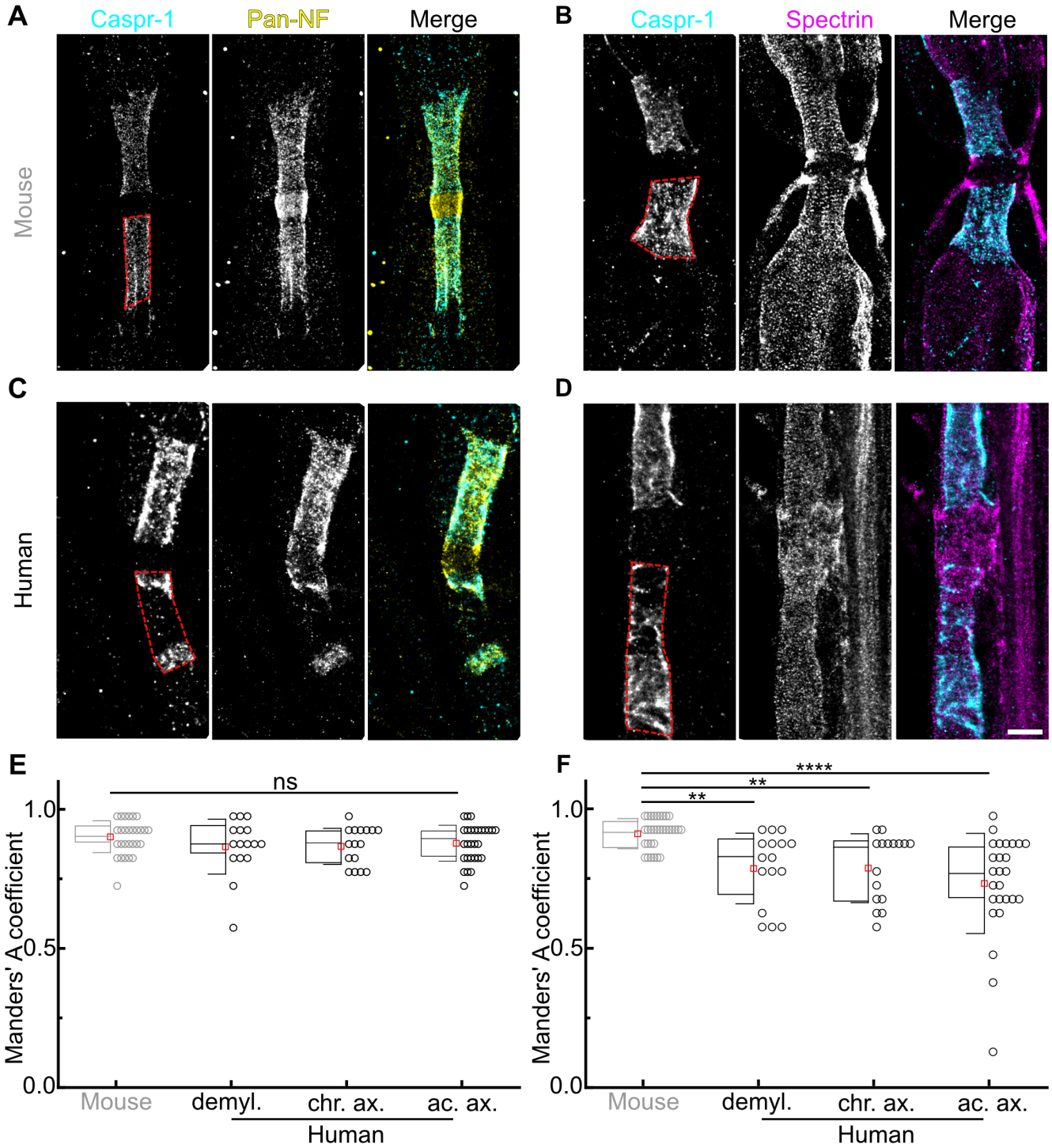

Fig. 3. Dual-color *d*STROM reveals partial loss of the junctional complex of Caspr-1/pan-neurofascin and disjunction from its cytoskeletal anchor protein ß2-spectrin in polyneuropathy. (A-D) Super-resolved image reconstruction show colocalization of Caspr-1 (cyan) and pan-neurofascin (Pan-NF, yellow; A, C) and Caspr-1 and ß2-spectrin (magenta; B, D) in murine (A-B) and human (C-D) teased fiber preparations. Exact colocalization appears white. Gaps within the paranodal Caspr-1/pan-neurofascin staining illustrate partial loss of the axoglial complex at the paranode in a patient with acute and severe axonal neuropathy (C). Note: neurofascin-staining in the nodal region was not considered in the analysis, as the pan-neurofascin antibody stains both paranodal neurofascin-155 and nodal neurofascin-186 isoform. Analysis was performed within the paranodal region only (red dashed line). (D) In areas of loss of axonal Caspr-1, ß2-spectrin staining is still present, but pathologically altered without clearly visible periodic arrangement. (E) Boxplots show the distribution of Manders' correlation coefficients between the axoglial complex Caspr-1 and neurofascin-155 in murine paranodes (n = 28) and paranodes of patients with demyelinating (demyl. n = 16), chronic axonal (chr.ax., n = 16) and acute axonal (ac.ax., n=28) neuropathy, without significant differences between the groups. (F) The distribution of Manders' correlation coefficients between axonal junctional Caspr-1 and cytoskeletal anchor protein ß2-spectrin in the same groups (n = 32 / 16 / 16 / 26 paranodes) show significantly decreased colocalization and thus a detachment of Caspr-1 from its anchor molecule, especially in the group of acute axonal neuropathies. Testing was performed using Kruskal-Wallis with Dunn's correction for multiple testing. Significance level: * $p < 0.05$, ** $p < 0.01$, *** $p < 0.001$, **** $p < 0.0001$. Boxplots display mean (red square), median (line), standard deviation (whiskers) and 25-75% (box). Scale bars 2 µm.

Category	node/tissue volume (1/mm^3)	paranodal axonal diameter (µm)	nodo-paranodal length (µm)	nodal length (µm)
intact human nodes	n.a.	2.3 ± 0.9.	10.0 ± 4.9.	0.9 ± 0.3.
acute axonal neuropathy	16.1 ± 3.5	2.3 ± 0.9 n.s.	15.4 ± 10.1 ***	1.3 ± 1.4 n.s.
chronic axonal neuropathy	33.3 ± 10.0	2.2 ± 0.9 n.s.	12.6 ± 7.1 ****	1.2 ± 2.0 n.s.
chronic demylenating neuropathy	35.9 ± 26.6	2.7 ± 1.0 **	12.9 ± 7.1 ****	1.1 ± 0.9 n.s.
murine sural nerve	77.2	1.9 ± 0.44 n.s.	8.8 ± 1.5 n.s.	1.1 ± 0.44 n.s.

Table 1. Nodo-paranodal morphometrics in murine and human sensory nerves - physiological and pathological conditions. The table displays means ± standard deviations (SD) of nodo-paranodal parameters (nodo-paranodal length, nodal length and paranodal axonal diameter) measured on Caspr-1 staining in human sural nerve intact nodes of Ranvier, and nodes of Ranvier of patients classified as acute axonal, chronic axonal and chronic demyelinating neuropathy (>180 nodes per cohort). Adjusted p-values are displayed compared to intact human nodes using Kruskal-Wallis test with Dunn's correction for multiple testing. Individual patient values and n numbers are displayed in Supplemental Table S5. Significance levels: * $p < 0.05$, ** $p < 0.01$, *** $p < 0.001$, **** $p < 0.0001$. Abbreviations: n.a = not applicable, n.s. = not significant, SD = standard deviation.

Physiological nodo-paranodal parameters in rodents and humans. As data are scarce, we firstly aimed at defining normal values of nodo-paranodal parameters in human adults. Therefore, we assessed and compared morphometrics in rodent and human sural nerves on morphologically intact nodes of Ranvier. The murine teased fiber preparations of sural nerve resembled fibers previously defined (40) as normal in humans: The thinnest myelinated fiber diameter was > 50% of the thickest, and no signs of paranodal disruption, segmental de- and remyelination, axonal degeneration including empty nerve strands were present (see 4A). Fibers thus represented healthy myelinated fibers (40) and representative n = 60 murine nodes of Ranvier within the samples were included in the analysis. When qualitatively assessing teased nerve fibers of patients with polyneuropathy, normal-looking nodes (similar to the nodes from murine teased fibers) and altered nodes (e.g. with asymmetric or uneven staining) were apparent. To define normal values in humans, we defined intact human nodes of Ranvier within the biopsy teased fiber preparations as following: 1) two opposing and symmetric Caspr-1 blocks, 2) homogeneous staining and 3) rectangular form. We selected and measured n = 69 intact looking nodes from presumably unaffected fibers from n = 4 patients of our cohort with mild neuropathy and only minor pathological alterations in the semithin sections (n = 1 demyelinating, n = 3 axonal; see Supplemental Table S5). For nodo-paranodal morphometrics, we assessed 1) the total length of two opposing Caspr-1 blocks including the nodal gap as an indicator of nodo-paranodal length, 2) the gap between two Caspr-1 blocks as an indicator of the nodal length and 3) the Caspr-1 diameter as an indicator of the paranodal axonal diameter (see Figure 4B & Supplemental Movie M1). The mean nodo-paranodal length was 10.0 ± 4.9 µm, mean nodal length in humans was 0.9 ± 0.3 µm and axonal paranodal diameter was 2.3 ± 0.9 µm, without any significant differences to murine sural nerve parameters (see Table 1). Thus, these values can be considered as normal values of unaltered nodes of Ranvier in adult humans.

Node of Ranvier density as a surrogate parameter for severity of axonal loss. To check whether the teased fiber samples represented type and severity of neuropathy as assessed by cross-sectional gold standard analysis, we measured the node of Ranvier density per tissue volume on each sample. Therefore, we aimed at implementing automated image analysis methods that could be translated to the diagnostic routine of teased fiber assessment in the future. We used computational image analysis to assess nodal count and tissue volume in an automated manner and FIJI-based segmentation combined with manual count of nodes of Ranvier as a manual control. In murine samples, we obtained a high counting accuracy of the fully automated nodal count (97 ± 11%; see Figure 4C) with a high correlation of the nodal count in single samples comparing fully automated and manual assessment (0.77, $p < 0.0001$). In pathologically altered human samples, the automated recognition had a reduced counting accuracy with a significantly increased variance ($F = 0.037$, $p < 0.0001$) due to the heterogeneity of pathological alterations (see Figure 4C). Therefore, node of Ranvier density was assessed and compared within patients using the FIJI-based routine. Patients with acute axonal neuropathy showed a significantly reduced nodal count compared to patients with chronic axonal neuropathy (16.1 vs. 33.3, $p = 0.015$). We found a strong correlation of the total count of nodes of Ranvier in our teased fiber samples with parameters assessed by gold standard cross-sectional analysis: Teased fiber node density correlated with the semi-quantitative rating of histopathological severity of axonal loss (Spearman $r = -0.75$, $p < 0.0001$), the mean fiber density as an exact quantification of histopathological severity of axonal loss (Spearman $r = 0.68$, $p = 0.002$, see Figure 4D) and with the mean count of Wallerian degeneration figures (Spearman $r = -0.54$, $p = 0.026$). A correlation of the teased fiber node of Ranvier density and sural nerve sensory nerve action potential amplitudes closely missed significance ($r = 0.41$, $p = 0.097$). Thus, we confirmed that our teased fiber preparations were representative of the histopathological diagnoses. Furthermore, we showed that the node of Ranvier density in teased fiber preparations measured via a semi-automated manner is a possible surrogate marker for severity of axonal loss.

Dispersion and loss of the paranodal junctional complex in patients with both axonal and demyelinating polyneuropathies. Next, we assessed and compared nodo-paranodal parameters in patients classified as acute axonal, chronic axonal and chronic demyelinating neuropathy, assessing > 180 single nodes per cohort. Although we found a significant increase in nodo-paranodal length in all three groups

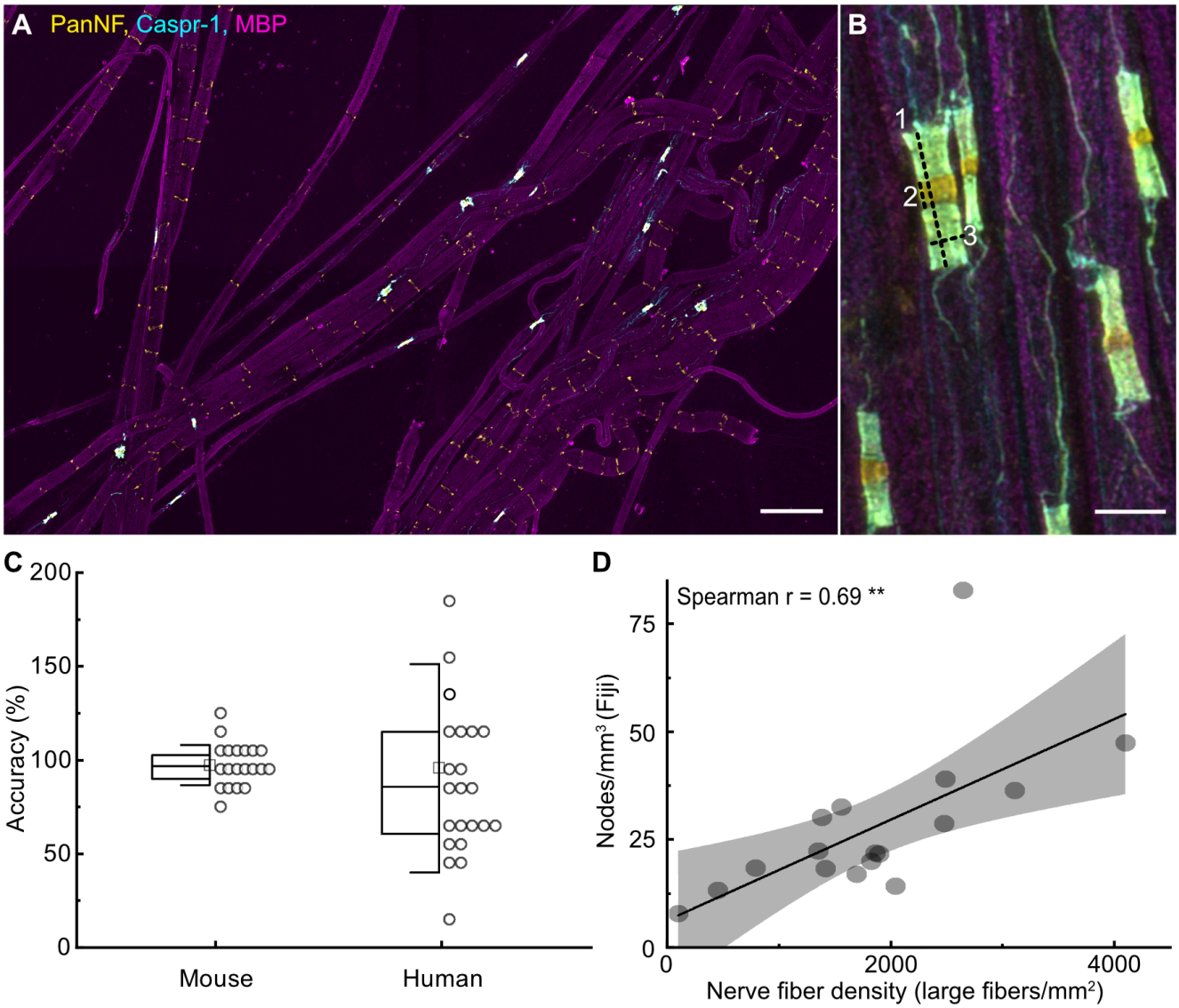

Fig. 4. Assessing nodo-paranodal morphometrics and nodal count in large field of view photomicrographs. (A) large field of view photomicrographs of bundle teased fiber preparations of murine sural nerves show healthy myelinated fibers (MBP staining, magenta) with nodes of Ranvier expressing neurofascin-155 and neurofascin-186 (pan-neurofascin, yellow) and Caspr-1 (cyan), with colocalization at the paranode (white). Scale bar = 50 µm. (B) Nodo-paranodal morphometrics including nodo-paranodal length (1), nodal length (2) and axonal diameter (3) were assessed as indicated. Scale bar = 5 µm. (C) Accuracy of automated vs. manual node of Ranvier counting are shown for murine samples and human samples. In murine samples, automated analysis resulted in highly accurate results, whereas accuracy in human samples was reduced due to pathological node of Ranvier alterations. (D) The scatter plot shows a positive correlation of the teased fiber node of Ranvier density assessed manually with FIJI and the nerve fiber density assessed by gold-standard cross-sectional analysis in the whole cohort (Pearson r = 0.69, p = 0.002). Significance level: * $p < 0.05$. ** $p < 0.01$, *** $p < 0.001$, **** $p < 0.0001$.

compared to intact human nodes (see Figure 5, A and B), we detected apparent differences within single patients and within histopathological categories: Patients with acute axonal damage showed significantly increased nodo-paranodal length compared to patients with chronic axonal polyneuropathy (15.6 vs. 12.4 µm, p = 0.002). Results closely missed significance compared to patients with demyelinating polyneuropathy (15.6 vs. 12.9 µm, p = 0.06, see Figure 5B). Additionally, nodo-paranodal length was significantly increased in patient samples with histopathologically severe axonal loss compared to histopathologically moderate axonal loss (16.8 vs 12.8, p = 0.0018) and histopathologically mild axonal loss (16.8 vs. 12.9, p = 0.0022, see Figure 5C). A negative correlation of nodo-paranodal length and large fiber density closely missed significance (Spearman r = -0.44, p = 0.078). Interestingly, single patients showed severe and highly significant nodo-paranodal alterations, especially in the cohort of acute axonal neuropathy, whereas other patients showed nodo-paranodal lengths without significant differences to normal values (individual data are shown in Supplemental Table S5). Relating our histopathological findings to clinical diagnoses, we also compared nodo-paranodal lengths between patients fulfilling diagnostic criteria for the two most frequent diseases within the cohort and different underlying pathophysiology: Vasculitic neuropathy with primarily axonal damage and distal Wallerian degeneration due to ischemia and CIDP with chronic, primarily demyelinating internodal myelin alterations. Here, we found a significant elongation of nodo-paranodal length measured via Caspr-1 staining in patients with vasculitic neuropathy compared to

chronic demyelinating disease (13.2 ± 6.8 vs. 12.3 ± 6.4 µm, p = 0.036). In conclusion, an increase in nodo-paranodal length measured via Caspr-1 staining was identified as an indicator for acute and severe axonal damage during Wallerian degeneration, and high inter-individual differences highlighted possible distinct underlying pathologies and the diagnostic potential of the method.

The nodal length did not differ between patient cohorts with acute, chronic axonal and demyelinating neuropathy compared to intact nodes, nor between patient cohorts with mild, moderate or severe axonal loss (see Table 1). Still, we found significant nodal elongations in single patients who were clinically severely affected (see Supplemental Table S3). In the whole cohort, the nodal length correlated to clinical motor function scores (mean nodal length vs. Overall disability sum score: Pearson r = 0.59, p = 0.01; mean nodal length vs. Medical Research Council Sum Score: Pearson r = -0.83, p < 0.0001), but not to histopathological severity of axonal loss. Most patients with axonal neuropathies showed normal paranodal axonal diameters (see Table 1 and Supplemental Table S5).

On the other hand, the paranodal diameter in patients with chronic demyelinating polyneuropathy was 2.7 µm and thus significantly increased compared to intact nodes, and compared to patients with acute and chronic axonal neuropathy (p < 0.0001). Thus, paranodal swelling was found to be prominent in patients with demyelinating neuropathies. We did not detect any correlation of clinical or histopathological disease severity and axonal diameter. In all analyses, age was considered as a possible confounder, but did not correlate to any of the measured parameters.

In conclusion, the results from the high-content analysis of teased fiber samples labeled with standard immunofluorescence add to and support our findings on an ultrastructural level assessed by super resolution *d*STORM microscopy: The nodes assessed by *d*STORM were representative within the samples and diagnostic categories, and we showed that nodo-paranodal alterations occur at a severe level especially in acute and severe axonal neuropathy. By *d*STORM analysis, we identified the alteration of the axonal cytoskeletal ultrastructure as a possible pathogenic link to dispersion and loss of the paranodal axoglial complex in acute axonal neuropathies.

Discussion

We implemented *d*STORM imaging as a method for nerve ultrastructural assessment in human tissue under pathological conditions. Thereby, we identified distinct pathologies on a nanoscale level in polyneuropathy: We demonstrate a physiological ∼190 nm periodic arrangement of the membrane-associated cytoskeleton in human ex vivo axons, and a disruption of this arrangement at the paranode in patients with polyneuropathy. Our data indicate that such disruption of cytoskeletal architecture as a nanostructural correlate of beginning Wallerian degeneration might facilitate nodo-paranodal detachment. By demonstrating pathologies on a nanoscale level in individual nodes of Ranvier and individual patients, we introduce single molecule localization microscopy as a potential method to enhance diagnostics of neurological diseases.

The ultrastructural paranodal protein arrangement is impaired in polyneuropathy. Here, we report an increase in periodic distance of the axoglial paranodal proteins Caspr-1 and neurofascin-155 in patients with polyneuropathies. These proteins are components of the axoglial septate-like junctions at the paranodal region and are crucial for the integrity of the node of Ranvier and saltatory conduction (2, 8, 9, 41, 42). Previous studies have proposed a helical arrangement of Caspr-1 along the axon, which evolves during the myelination process and Schwann cell wrapping (43–45). We now hypothesize that the lateral increase in the periodic distance of Caspr-1 in polyneuropathy is a correlate of a lateral decoiling of the axonal Caspr-1 helices under pathological conditions. We then addressed the question of origin of this pathology.

Dual-color super-resolution imaging reveals distinct pathomechanisms of paranodal disjunction. Our data from colocalization studies based on *d*STORM images show that the axoglial complex of Caspr-1 and neurofascin-155 itself is robust against disjunction. We could show that paranodal axoglial contact of axonal Caspr-1 with its glial counterpart neurofascin-155 remains intact, even in pathologically altered paranodes. Previous studies using Shiverer mutant mice, a murine model to study demyelinating disease, have shown a close attachment of Caspr-1 to neurofascin-155, even if not concentrated at the axoglial junctions (10). Rodent cell culture studies also showed that during the myelination process, Caspr-1 and neurofascin-155 move "in perfect register with each other" along the axon (44). Our data now confirm that even in pathologically altered nerves, this close association of the axoglial complex remains intact. We observed either normal paranodal axoglial arrangement, equally increased periodicity or a partial loss of both proteins in parallel. These findings imply that the disruption of the nodo-paranodal architecture in axonal neuropathy does not occur due to a primary disjunction of the axoglial contact.

Importantly, our data indicate that the paranodal region constitutes an Achilles' heel for cytoskeletal damage in axonal neuropathies. At the internode, we found no differences on internodal ß2-spectrin periodicity between humans and rodents. Our data thus are in line with previous studies that postulated that the axoskeletal ultrastructure is conserved within species (46) and also suggest that the internodal region is less prone to axoskeletal pathology. At the paranode, on the other hand, we observed an increase in periodic arrangement of ß2-spectrin in patients with polyneuropathy compared to rodents. We exclusively studied ß2-spectrin, as other cytoskeletal proteins like F-actin and ankyrin B are also present in the paranodal glial terminal loops, and their complex 3D structure thus impede the analysis of axonal periodicity (20, 47).

The paranodal region might be prone to cytoskeletal alterations for two main reasons: Firstly, the axon diameter is reduced physiologically in the paranodal region, axoskeletal

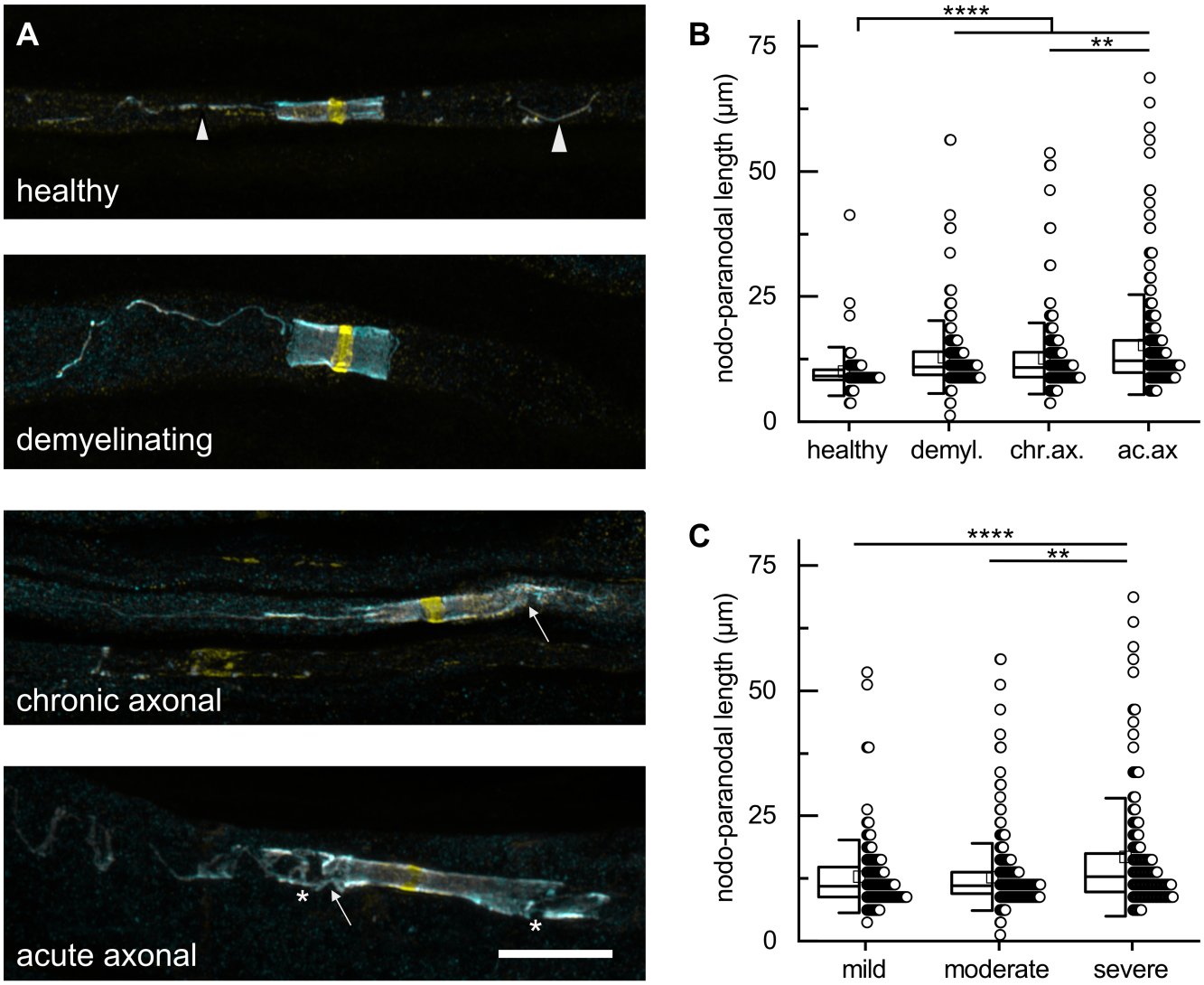

Fig. 5. Nodo-paranodal length is elongated with patients with acute and severe axonal neuropathy. (A) High magnification photomicrographs show node and paranode morphology in human nodes of Ranvier considered as unaltered and in patients classified as demyelinating, chronic axonal and acute axonal neuropathy. In physiological nodes, paranodal Caspr-1 (cyan) and neurofascin (yellow) are dense, and the mesaxon can be distinguished clearly (arrowheads). In patients with chronic and acute axonal neuropathy, paranodal elongation with decoiling of paranodal axoglial proteins (arrows) and partial loss of staining (asterisks) is visible. Correspondingly to results of *d*STORM analysis, Caspr-1 and neurofascin colocalize at the paranode (white), even in pathologically severely altered nodes of Ranvier. Scale bar = 10µm. (B) Nodo-paranodal length (µm, y-axis) is elongated in patients with all types of polyneuropathies compared to unaltered human nodes, especially in patients with acute axonal neuropathy. (C) Nodo-paranodal length (µm, y-axis) is elongated in patients with histopathologically severe axonal loss, compared to mild and moderate axonal loss. Testing was performed using Kruskal-Wallis with Dunn's correction for multiple testing. Significance level: * $p < 0.05$. ** $p < 0.01$, *** $p < 0.001$, **** $p < 0.0001$.

transport proteins are condensed and axonal transport rates are reduced (4, 48). Endogenous metabolites could therefore accumulate, leading to axoskeletal damage. Secondly, the node of Ranvier of myelinated fibers is the region that is least protected by the myelin sheath and thus exposed to exogenous noxious and inflammatory agents. Further evidence supports the hypothesis of vulnerability of the paranode: In toxic neuropathies and animal models, paranodal swelling has been observed due to a cross-linking of cytoskeletal proteins (49–51). Furthermore, electron microscopy studies in animals have shown that early Wallerian degeneration begins at the nodal and paranodal axon, with accumulation of cell organelles and loosening of neurofilaments (52–54). We show that the paranodal and nodal axon is the initial site of Wallerain degeneration in human disease, and provide evidence for specific cytoskeletal alterations at a nanoscale and protein level in patients with axonal neuropathy as a correlate of a beginning Wallerian degeneration. In demyelinating neuropathies, we found mild alterations of the cytoskeleton, though not significantly different from murine healthy paranodes. Our "real world" cohort is small and heterogeneous, and patients with primary demyelinating disease also show histopathological and electrophysiological signs of secondary axonal damage. Furthermore, distinction between axonal and demyelinating disease was based on the histopathological assessment, not considering the underlying etiology of the disease. We therefore hypothesize that alterations of the paranodal axonal cytoskeleton can be found in demyelinating neuropathies due to secondary axonal damage and do not reflect pathomechanisms occuring in primary demyeli-

nating disease.

Super-resolution imaging visualizes the link of paranodal detachment with cytoskeletal damage. Our findings imply that in axonal neuropathies, the paranodal cytoskeletal damage might be associated with the nodo-paranodal detachment. Previous studies suggest that paranodal ß2-spectrin serves as an intra-axonal barrier at the paranode, and that α2/ß2-spectrin is crucial for the clustering of sodium channels at the node (55, 56).

Furthermore, *d*STORM data revealed that the concentration of ß2-spectrin is the key factor to form and maintain the periodicity of the membrane-associated cytoskeleton (34). The maintenance of its periodic cytoskeletal arrangement is crucial for axonal survival, and full spectrin-knockout models are lethal (34, 56). We now can show that along with the alteration of the axonal cytoskeleton, the colocalization of Caspr-1 and its axonal anchor molecule ß2-spectrin is severely disrupted. This finding implies the following hypothesis: The alteration of cytoskeletal structure proteins might lead to a lateral de-coiling of the Caspr-1 helices along the axon. This is in line with reports of a paranodal disorganization and decreased expression levels of Caspr-1 in protein 4.1B murine knock-out models (36, 57–59). As the strong association of Caspr-1 and glial Neurofascin-155 remains intact, a broadening of the paranodal loops would be the result. In more severe stages of axonal damage, a loss of axonal proteins of the septate junction might lead to a detachment of the terminal myelin loop from the axon and a consecutive complete destruction of the paranodes. This notion is supported by the correlation of nodo-paranodal length to histopathological severity and acuteness of axonal loss in our cohort. Furthermore, our findings are in line with previous reports on paranodal detachment in other neuropathies histopathologically and electrophysiologically showing axonal features, such as diabetic neuropathy and chronic idiopathic axonal polyneuropathy (18, 60–63). On a nanostructural level, previous studies in rats showed that during Wallerian degeneration, myelin and terminal loop alterations occur only after axonal cytoskeletal changes (52, 54). Thus, our data indicate that a paranodal elongation and disruption may rather be considered a secondary effect of axonal damage than a primarily demyelinating feature in axonal neuropathy caused by acute Wallerian degeneration in patients with polyneuropathy. Although we observed a partial loss of Caspr-1 at the paranodes in our patients, the conditional murine knockout of single axoskeletal molecules, even ß2-spectrin, does not lead to a complete detachment of Caspr-1, previously shown by using diffraction-limited microscopy (3, 55). We therefore suggest that a paranodal disjunction in axonal neuropathy occurs in case of a severe disruption of the axonal cytoskeleton involving several structure proteins at a time, and can better be observed using SMLM.

Further studies are needed to address various cytoskeletal proteins, especially investigating the role of protein 4.1B (37, 58, 59), which was not included in the study due to a lack of a commercial antibody apt for super resolution microscopy. A combination of electron microscopy with super-resolution microscopy techniques (24, 64, 65) might confirm and further investigate the underlying histopathological changes. Furthermore, the effect of cytoskeletal damage on nodal ion channels needs to be further investigated on a nanoscale level in future studies.

Paranodal detachment in axonal neuropathy differs from autoimmune nodo-paranodopathy and demyelinating neuropathy. The pathomechanism of nodo-paranodal disruption in axonal neuropathies we propose within this study is different to previously suggested mechanisms of nodo–paranododal disruption in autoantibody-mediated nodo-paranodopathy. This rare disease is an autoimmune neuropathy associated with pathogenic autoantibodies against proteins located at the node of Ranvier, which attack proteins of the axoglial junction. As a consequence, a primary axoglial detachment induced by the autoantibodies has been proposed, either by directly inhibiting the interaction of axonal and glial binding partners or by altered myelin turnover (63, 66–69). However, our cohort does not include patients with this rare disease, as today, antibodies serve as a biomarker and reduce the need for invasive diagnostic procedures. Additionally, nodal elongations measured by the gap of myelin basic protein have also been described in skin biopsies of patients with chronic inflammatory demyelinating neuropathy (70–72). In this study, we found paranodal elongations measured by Caspr-1 staining in patients with acute axonal neuropathy to be significantly longer than in CIDP. Still, our CIDP cohort is small and not typical, as diagnosis of CIDP usually does not need nerve biopsy and is only performed in unclear cases. We thus cannot directly compare these possible mechanisms of axoglial disjunction. Still, we hypothesize that in axonal neuropathies, the axoglial complex remains intact, but detaches from its cytoskeletal anchor, whereas autoimmune nodopathies lead to a axoglial detachment (11, 67, 69, 73, 74). The methods described in this study yield the opportunity to investigate and directly compare different mechanisms of paranodal damage on a nanostructural scale in future studies, e.g. including cell-culture-based assays.

Advanced high- and super-resolution microscopy pushes the boundaries of diagnostic assessment of nerve biopsies in polyneuropathies. Using a high-content confocal imaging approach, we were able to confirm our findings on an ultra-structural level in high sample sizes of nodes of Ranvier. Additionally, our protocol of teased fiber preparation and high-content confocal assessment may provide further means in the diagnostic work-up of polyneuropathies. To date, the gold-standard histopathological techniques using cross sections (40, 71, 75) do not allow detailed examination of nodes of Ranvier, although its assessment has gained importance (15). Supplemental methods to exclusively assess the node of Ranvier are sensory nerve single teased fiber analysis (40, 49, 71, 76–78), electron microscopy including longitudinal sections (53, 69, 71, 74, 75, 79) and analysis of myelinated fibers in skin biopsies (71, 72, 80). In the latter, standard values for nodal length measured via

myelin basic protein gaps have been established and have been shown to be elongated in both axonal and demyelinating disease (60, 72, 81). Still, these methods can be time-consuming, require high expertise due to non-standardized assessment, depend on rater-dependent accuracy and partly do not allow to specifically study single proteins of interest (40, 71, 72, 76, 82). Here, we introduce a different protocol including fiber bundle teasing that can be performed within 60 minutes, followed by triple immunofluorescence staining and automated confocal high-content image acquisition. This method yields the opportunity to combine the advantages of the methods mentioned above: To assess internodal myelin pathology in longitudinal fibers and to study numerous nodes of Ranvier or any other specific target structure of the peripheral sensory nerve at high magnification using target-specific immunofluorescence staining. As *d*STORM imaging routines enable the identification of pathological alterations in individual patients' nodes of Ranvier at the nanoscale, in future our method could address additional targets in larger cohorts involving myelin pathology and distinct axonal markers. Even beyond nerve biopsies, less invasive skin biopsies diagnostics could further push the boundaries.

Furthermore, high-content analysis and implementation of segmentation methods helps to minimize selection-bias by the examiner. Segmentation techniques and analysis applying deep learning algorithms have been applied not only in SLML applications, but also on rodent and porcine peripheral nerve and human healthy CNS cross sections (56, 83–86). Here, we could implement automated segmentation on murine healthy samples, and integrate image segmentation in the analysis of human histopathological samples, though not in a fully automated-manner. We thereby identified the node of Ranvier density as a surrogate marker for axonal loss in teased fiber preparations. This yields the opportunity to assess both severity of axonal neuropathy and node of Ranvier pathology using one single method, including semi-automated analysis. Most recently, super resolution microscopy and image segmentation was successfully implemented on healthy human peripheral nerve cross sections (87). With further technological advances, deep learning algorithms could be used to assess nodes of Ranvier including pathological changes, and additional histopathologic parameters. Thus, we believe that in the future, modern image analysis and quantification approaches add to the histopathological gold standard techniques when assessing histopathology in polyneuropathy. Additionally, we now provide standardized normal values of human adult sensory nerve nodo-paranodal length and diameter determined by Caspr-1 staining. The methodology including nodo-paranodal morphometrics presented in this study could be used for diagnostic assessment in the future.

Here we show that nodo-paranodal length and diameter do not differ in human and rodent healthy nodes of peripheral sensory axons. Our data on physiological nodal length are in line with previous reports in children and adolescents (88). Unfortunately, we cannot address yet to what extent internodal and nodo-paranodal changes are physiological and occur with age in the elderly due to a lack of human healthy controls due to ethical reasons, as post-mortem autopsy material as a control might not be suited due to immediate and early post-mortem cytoskeletal and structural alterations (89). Still, we did not observe a correlation of age to nodo-paranodal parameters, arguing against age being a confounder in the analysis. Despite a small sample size, we identify paranodal swelling as exclusive for demyelinating disease, as previously described in avian models of demyelination and in patients with multiple sclerosis (90, 91). Furthermore, we find nodal elongation in single patients as a possible indicator of clinically severe demyelinating disease, corresponding to previous reports on nodal elongations in patients with in CIDP (70). Nodo-paranodal elongation measured via Caspr-1 staining, on the other hand, was not observed in demyelinating disease, but rather correlated to acute and severe axonal loss. Interestingly, patients with primarily axonal pathology such as vasculitic neuropathy showed an increased nodo-paranodal length compared to CIDP, a disease characterized by internodal demyelination. Previously, Caspr-1 staining was proposed as a diagnostic marker to distinguish chronic idiopathic axonal neuropathy from CIDP, and results show disorganization of Caspr-1 at the paranode in axonal neuropathy and thus are in line with our findings on nodo-paranodal length determined via Caspr-1 staining (18).

Using *d*STORM, we could show possible underlying mechanisms of Caspr-1 elongation and loss in axonal neuropathy. Our findings highlight the potential of advanced high and super-resolution microscopy for diagnostics and pathophysiological studies. Larger studies with homogenous cohorts need to confirm if nodo-paranodal morphometrics and ultrastructural assessment via *d*STORM can serve as diagnostic markers and assess their sensitivity, specificity and practicability in routine assessment. Our data contribute to the understanding of underlying node of Ranvier pathologies of peripheral neuropathies on a nanoscale level, with possible implications on diagnosis and possibly future treatment. Our findings could pave the way for introducing new imaging techniques and super resolution microscopy into histopathologic diagnostic assessment of patients with neurologic conditions.

Data availability. Data as described above are available here: https://doi.org/10.5281/zenodo.6387771. Further raw data including original photomicrographs and simulations will be available upon request by any qualified researcher.

Study approval. The study was approved by the institutional ethical committee (approval number 277/13 and 15/19). All subjects gave written informed consent prior to participation.

ACKNOWLEDGEMENTS

The study was supported by a grant of the Interdisciplinary Center of Clinical Research (IZKF) of the Medical Faculty of Würzburg to K.D. and K.G.H (F-N-439). J.L. was supported by a scholarship of the Graduate School of Life Sciences (GSLS) of the University of Würzburg. H.S.H. was supported by the Rudolf-Virchow-Center of the University of Würzburg. L.A. and K.D. hold research fellowships by the Interdisciplinary Center of Clinical Research (IZKF) of the Medical Faculty of Würzburg. We thank Antonia Kohl and Barbara Reuter for excellent technical assistance and

A. Balakrishnan and paraphrasis.de for proof-reading. We thank the patients and animals who contributed to the study.

EXTENDED AUTHOR INFORMATION

- Luise Appeltshauser: 0000-0001-5248-4009; LAppeltshauser
- Janis Linke: 0000-0002-4943-4542;
- Hannah S. Heil: 0000-0003-4279-7022; Hannah_SuperRes
- Christine Karus
- Joachim Schenk
- Katherina Hemmen
- Claudia Sommer: 0000-0002-7064-5002;
- Kathrin Doppler: 0000-0003-2883-0009
- Katrin G. Heinze: 0000-0003-2372-6800 @HeinzeLab

AUTHOR CONTRIBUTIONS

Author roles were defined according to criteria of the International Committee of Medical Journal Editors (92). K.G.H., K.D., L.A. and H.S.H conceived and designed the experiments. H.S.H. developed the image-correlation analysis routine. J.L. and C.K. performed the sample preparation, imaging and data analysis. J.S. performed the image segmentation and analysis of the AiryScan data. K.D. assessed histopathological features. L.A. assessed clinical data and analyzed clinical and histopathological data. L.A., H.S.H, and J.L. wrote the first draft of the manuscript. Order of co-first authors was decided on according to recently published recommendations (93), regarding each co-first author's role in the interpretation of the data and role in manuscript drafting. C.S., K.G.H., and K.D. revised the manuscript for scientific content. All authors read and approved the final manuscript.

COMPETING FINANCIAL INTERESTS

The authors declare no competing financial interests.

Bibliography

1. A. F. Huxley and R. Stämpeli. Evidence for saltatory conduction in peripheral myelinated nerve fibres. 108(3):315–339. ISSN 00223751. doi: 10.1113/jphysiol.1949.sp004335.
2. Matthew N. Rasband and Elior Peles. The nodes of ranvier: Molecular assembly and maintenance. 8(3):a020495. ISSN 1943-0264. doi: 10.1101/cshperspect.a020495.
3. Aniket Ghosh, Diane L. Sherman, and Peter J. Brophy. The axonal cytoskeleton and the assembly of nodes of ranvier. 24(2):104–110. ISSN 1073-8584, 1089-4098. doi: 10.1177/1073858417710897.
4. James L. Salzer. Schwann cell myelination. 7(8):a020529. ISSN 1943-0264. doi: 10.1101/cshperspect.a020529.
5. E. J. Arroyo and S. S. Scherer. On the molecular architecture of myelinated fibers. 113(1): 0001. ISSN 09486143. doi: 10.1007/s004180050001.
6. Catherine Faivre-Sarrailh and Jérôme J. Devaux. Neuro-glial interactions at the nodes of ranvier: implication in health and diseases. 7. ISSN 1662-5102. doi: 10.3389/fncel.2013.00196.
7. Konstantin Feinberg, Yael Eshed-Eisenbach, Shahar Frechter, Veronique Amor, Daniela Salomon, Helena Sabanay, Jeffrey L. Dupree, Martin Grumet, Peter J. Brophy, Peter Shrager, and Elior Peles. A glial signal consisting of gliomedin and NrCAM clusters axonal na+ channels during the formation of nodes of ranvier. 65(4):490–502. ISSN 08966273. doi: 10.1016/j.neuron.2010.02.004.
8. Catherine Faivre-Sarrailh. Molecular organization and function of vertebrate septate-like junctions. 1862(5):183211. ISSN 00052736. doi: 10.1016/j.bbamem.2020.183211.
9. Manzoor A. Bhat, Jose C. Rios, Yue Lu, German P. Garcia-Fresco, William Ching, Mary St. Martin, Jingjun Li, Steven Einheber, Mitchell Chesler, Jack Rosenbluth, James L. Salzer, and Hugo J. Bellen. Axon-glia interactions and the domain organization of myelinated axons requires neurexin IV/caspr/paranodin. 30(2):369–383. ISSN 08966273. doi: 10.1016/S0896-6273(01)00294-X.
10. Steven Tait, Frank Gunn-Moore, J. Martin Collinson, Jeffery Huang, Catherine Lubetzki, Liliana Pedraza, Diane L. Sherman, David R. Colman, and Peter J. Brophy. An oligodendrocyte cell adhesion molecule at the site of assembly of the paranodal axo-glial junction. 150(3):657–666. ISSN 0021-9525, 1540-8140. doi: 10.1083/jcb.150.3.657.
11. Jean-Michel Vallat, Mathilde Nizon, Alex Magee, Bertrand Isidor, Laurent Magy, Yann Péréon, Laurence Richard, Robert Ouvrier, Benjamin Cogné, Jérôme Devaux, Stephan Zuchner, and Stéphane Mathis. Contactin-associated protein 1 (*CNTNAP1*) mutations induce characteristic lesions of the paranodal region. 75(12):1155–1159, . ISSN 0022-3069, 1554-6578. doi: 10.1093/jnen/nlw093.
12. R. Hanewinckel, M.A. Ikram, and P.A. Van Doorn. Peripheral neuropathies. In *Handbook of Clinical Neurology*, volume 138, pages 263–282. Elsevier. ISBN 978-0-12-802973-2. doi: 10.1016/B978-0-12-802973-2.00015-X.
13. Claudia Sommer, Christian Geber, Peter Young, Raimund Forst, Frank Birklein, and Benedikt Schoser. Polyneuropathies. 115(6):83–90. ISSN 1866-0452. doi: 10.3238/arztebl.2018.083.
14. Antonino Uncini, Keiichiro Susuki, and Nobuhiro Yuki. Nodo-paranodopathy: Beyond the demyelinating and axonal classification in anti-ganglioside antibody-mediated neuropathies. 124(10):1928–1934, . ISSN 13882457. doi: 10.1016/j.clinph.2013.03.025.
15. Antonino Uncini, Stephane Mathis, and Jean-Michel Vallat. New classification of autoimmune neuropathies based on target antigens and involved domains of myelinated fibres. 93(1):57–67, . ISSN 0022-3050, 1468-330X. doi: 10.1136/jnnp-2021-326889.
16. Janev Fehmi, Steven S Scherer, Hugh J Willison, and Simon Rinaldi. Nodes, paranodes and neuropathies. 89(1):61–71. ISSN 0022-3050, 1468-330X. doi: 10.1136/jnnp-2016-315480.
17. Keiichiro Susuki. Node of ranvier disruption as a cause of neurological diseases. 5(3): AN20130025. ISSN 1759-0914, 1759-0914. doi: 10.1042/AN20130025.
18. Carmen Cifuentes-Diaz, Odile Dubourg, Theano Irinopoulou, Marc Vigny, Sylvie Lachkar, Laurence Decker, Patrick Charnay, Natalia Denisenko, Thierry Maisonobe, Jean-Marc Léger, Karine Viala, Jean-Jacques Hauw, and Jean-Antoine Girault. Nodes of ranvier and paranodes in chronic acquired neuropathies. 6(1):e14533, . ISSN 1932-6203. doi: 10.1371/journal.pone.0014533.
19. Jörn Heine, Matthias Reuss, Benjamin Harke, Elisa D'Este, Steffen J. Sahl, and Stefan W. Hell. Adaptive-illumination STED nanoscopy. 114(37):9797–9802. ISSN 0027-8424, 1091-6490. doi: 10.1073/pnas.1708304114.
20. Elisa D'Este, Dirk Kamin, Francisco Balzarotti, and Stefan W. Hell. Ultrastructural anatomy of nodes of ranvier in the peripheral nervous system as revealed by STED microscopy. 114(2):E191–E199, . ISSN 0027-8424, 1091-6490. doi: 10.1073/pnas.1619553114.
21. Christophe Leterrier. Putting the axonal periodic scaffold in order. 69:33–40. ISSN 09594388. doi: 10.1016/j.conb.2020.12.015.
22. Christophe Leterrier, Pankaj Dubey, and Subhojit Roy. The nano-architecture of the axonal cytoskeleton. 18(12):713–726. ISSN 1471-003X, 1471-0048. doi: 10.1038/nrn.2017.129.
23. Ke Xu, Guisheng Zhong, and Xiaowei Zhuang. Actin, spectrin, and associated proteins form a periodic cytoskeletal structure in axons. 339(6118):452–456, . ISSN 0036-8075, 1095-9203. doi: 10.1126/science.1232251.
24. Stéphane Vassilopoulos, Solène Gibaud, Angélique Jimenez, Ghislaine Caillol, and Christophe Leterrier. Ultrastructure of the axonal periodic scaffold reveals a braid-like organization of actin rings. 10(1):5803. ISSN 2041-1723. doi: 10.1038/s41467-019-13835-6.
25. Markus Sauer and Mike Heilemann. Single-molecule localization microscopy in eukaryotes. 117(11):7478–7509. ISSN 0009-2665, 1520-6890. doi: 10.1021/acs.chemrev.6b00667.
26. Mike Heilemann, Sebastian vandeLinde, Anindita Mukherjee, and Markus Sauer. Super-resolution imaging with small organic fluorophores. 48(37):6903–6908. ISSN 14337851, 15213773. doi: 10.1002/anie.200902073.
27. Christian M. Winterflood, Evgenia Platonova, David Albrecht, and Helge Ewers. Dual-color 3d superresolution microscopy by combined spectral-demixing and biplane imaging. 109 (1):3–6. ISSN 00063495. doi: 10.1016/j.bpj.2015.05.026.
28. Guillaume Jacquemet, Alexandre F. Carisey, Hellyeh Hamidi, Ricardo Henriques, and Christophe Leterrier. The cell biologist's guide to super-resolution microscopy. 133(11). ISSN 0021-9533. doi: 10.1242/jcs.240713.
29. Christian Werner, Martin Pauli, Sören Doose, Andreas Weishaupt, Holger Haselmann, Benedikt Grünewald, Markus Sauer, Manfred Heckmann, Klaus V. Toyka, Esther Asan, Claudia Sommer, and Christian Geis. Human autoantibodies to amphiphysin induce defective presynaptic vesicle dynamics and composition. 139(2):365–379. ISSN 1460-2156, 0006-8950. doi: 10.1093/brain/awv324.
30. Florian Levet, Guillaume Julien, Rémi Galland, Corey Butler, Anne Beghin, Anaël Chazeau, Philipp Hoess, Jonas Ries, Grégory Giannone, and Jean-Baptiste Sibarita. A tessellation-based colocalization analysis approach for single-molecule localization microscopy. 10(1):2379. ISSN 2041-1723. doi: 10.1038/s41467-019-10007-4.
31. Alistair P. Curd, Joanna Leng, Ruth E. Hughes, Alexa J. Cleasby, Brendan Rogers, Chi H. Trinh, Michelle A. Baird, Yasuharu Takagi, Christian Tiede, Christian Sieben, Suliana Manley, Thomas Schlichthaerle, Ralf Jungmann, Jonas Ries, Hari Shroff, and Michelle Peckham. Nanoscale pattern extraction from relative positions of sparse 3d localizations. 21 (3):1213–1220. ISSN 1530-6984, 1530-6992. doi: 10.1021/acs.nanolett.0c03332.
32. Elisa D'Este, Dirk Kamin, Caroline Velte, Fabian Göttfert, Mikael Simons, and Stefan W. Hell. Subcortical cytoskeleton periodicity throughout the nervous system. 6(1):22741, . ISSN 2045-2322. doi: 10.1038/srep22741.
33. Sven C. Sidenstein, Elisa D'Este, Marvin J. Böhm, Johann G. Danzl, Vladimir N. Belov, and Stefan W. Hell. Multicolour multilevel STED nanoscopy of actin/spectrin organization at synapses. 6(1):26725. ISSN 2045-2322. doi: 10.1038/srep26725.
34. Guisheng Zhong, Jiang He, Ruobo Zhou, Damaris Lorenzo, Hazen P Babcock, Vann Bennett, and Xiaowei Zhuang. Developmental mechanism of the periodic membrane skeleton in axons. 3:e04581. ISSN 2050-084X. doi: 10.7554/eLife.04581.
35. Nicolas Unsain, Martin D. Bordenave, Gaby F. Martinez, Sami Jalil, Catalina von Bilderling, Federico M. Barabas, Luciano A. Masullo, Aaron D. Johnstone, Philip A. Barker, Mariano Bisbal, Fernando D. Stefani, and Alfredo O. Cáceres. Remodeling of the actin/spectrin membrane-associated periodic skeleton, growth cone collapse and f-actin decrease during axonal degeneration. 8(1):3007. ISSN 2045-2322. doi: 10.1038/s41598-018-21232-0.
36. Y. Ogawa. Spectrins and AnkyrinB constitute a specialized paranodal cytoskeleton. 26 (19):5230–5239. ISSN 0270-6474, 1529-2401. doi: 10.1523/JNEUROSCI.0425-06.2006.
37. I. Horresh, V. Bar, J. L. Kissil, and E. Peles. Organization of myelinated axons by caspr and caspr2 requires the cytoskeletal adapter protein 4.1b. 30(7):2480–2489. ISSN 0270-6474, 1529-2401. doi: 10.1523/JNEUROSCI.5225-09.2010.
38. E. M. M. Manders, F. J. Verbeek, and J. A. Aten. Measurement of co-localization of objects in dual-colour confocal images. 169(3):375–382. ISSN 00222720. doi: 10.1111/j.1365-2818.1993.tb03313.x.
39. Kenneth W. Dunn, Malgorzata M. Kamocka, and John H. McDonald. A practical guide to evaluating colocalization in biological microscopy. 300(4):C723–C742. ISSN 0363-6143, 1522-1563. doi: 10.1152/ajpcell.00462.2010.
40. Peter J. Dyck, P. James B. Dyck, and Janean Engelstad. Pathologic alterations of nerves. In *Peripheral Neuropathy*, pages 733–829. Elsevier, . ISBN 978-0-7216-9491-7. doi: 10.1016/B978-0-7216-9491-7.50035-1.
41. Diane L. Sherman, Steven Tait, Shona Melrose, Richard Johnson, Barbara Zonta, Felipe A. Court, Wendy B. Macklin, Stephen Meek, Andrew J.H. Smith, David F. Cottrell, and Peter J. Brophy. Neurofascins are required to establish axonal domains for saltatory conduction. 48(5):737–742. ISSN 08966273. doi: 10.1016/j.neuron.2005.10.019.
42. Anilkumar M. Pillai, Courtney Thaxton, Alaine L. Pribisko, Jr-Gang Cheng, Jeffrey L. Dupree, and Manzoor A. Bhat. Spatiotemporal ablation of myelinating glia-specific *neurofascin* (nfasc ^{nf155}) in mice reveals gradual loss of paranodal axoglial junctions and concomitant disorganization of axonal domains. 87(8):1773–1793. ISSN 03604012, 10974547. doi: 10.1002/jnr.22015.
43. Jack Rosenbluth, Amanda Mierzwa, and Seema Shroff. Molecular architecture of myelinated nerve fibers: Leaky paranodal junctions and paranodal dysmyelination. 19(6):629–

641. ISSN 1073-8584, 1089-4098. doi: 10.1177/1073858413504627.
44. Liliana Pedraza, Jeffrey K. Huang, and David Colman. Disposition of axonal caspr with respect to glial cell membranes: Implications for the process of myelination. 87(15):3480–3491. ISSN 03604012, 10974547. doi: 10.1002/jnr.22004.
45. Menahem Eisenbach, Elena Kartvelishvily, Yael Eshed-Eisenbach, Trent Watkins, Annette Sorensen, Christine Thomson, Barbara Ranscht, Susan C. Barnett, Peter Brophy, and Elior Peles. Differential clustering of caspr by oligodendrocytes and schwann cells. 87(15): 3492–3501. ISSN 03604012, 10974547. doi: 10.1002/jnr.22157.
46. Jiang He, Ruobo Zhou, Zhuhao Wu, Monica A. Carrasco, Peri T. Kurshan, Jonathan E. Farley, David J. Simon, Guiping Wang, Boran Han, Junjie Hao, Evan Heller, Marc R. Freeman, Kang Shen, Tom Maniatis, Marc Tessier-Lavigne, and Xiaowei Zhuang. Prevalent presence of periodic actin–spectrin-based membrane skeleton in a broad range of neuronal cell types and animal species. 113(21):6029–6034. ISSN 0027-8424, 1091-6490. doi: 10.1073/pnas.1605707113.
47. Kae-Jiun Chang, Daniel R Zollinger, Keiichiro Susuki, Diane L Sherman, Michael A Makara, Peter J Brophy, Edward C Cooper, Vann Bennett, Peter J Mohler, and Matthew N Rasband. Glial ankyrins facilitate paranodal axoglial junction assembly. 17(12):1673–1681. ISSN 1097-6256, 1546-1726. doi: 10.1038/nn.3858.
48. A. Reles and R. L. Friede. Axonal cytoskeleton at the nodes of ranvier. 20(6):450–458. ISSN 0300-4864, 1573-7381. doi: 10.1007/BF01252273.
49. Brad Bolon, Ingrid D. Pardo, and Georg J. Krinke. The science and art of nerve fiber teasing for myelinated nerves: Methodology and interpretation. 48(1):49–58. ISSN 0192-6233, 1533-1601. doi: 10.1177/0192623319850773.
50. Sezin Alpaydin Baslo, Oya Ozturk, Cengiz Dayan, Dilek Atakli, and Mehmet Baris Baslo. Another brick in the wall: is hexane neuropathy a 'nodo-paranodopathy'? 121(2):373–378. ISSN 0300-9009, 2240-2993. doi: 10.1007/s13760-019-01137-z.
51. Tomoko Ishibashi and Hiroko Baba. Paranodal axoglial junctions, an essential component in axonal homeostasis. 10:951809. ISSN 2296-634X. doi: 10.3389/fcell.2022.951809.
52. R. H. M. Ballin and P. K. Thomas. Changes at the nodes of ranvier during wallerian degeneration: an electron microscope study. 14(3):237–249. ISSN 0001-6322, 1432-0533. doi: 10.1007/BF00685303.
53. P. H. Abrahams, A. Day, and G. Allt. The node of ranvier in early wallerian degeneration: A freeze-fracture study. 54(2):95–100. ISSN 0001-6322, 1432-0533. doi: 10.1007/BF00689401.
54. F.L. Mastaglia, W.I. McDonald, and K. Yogendran. Nodal changes during the early stages of wallerian degeneration of central nerve fibres. 30(2):259–267. ISSN 0022510X. doi: 10.1016/0022-510X(76)90132-5.
55. Veronique Amor, Chuansheng Zhang, Anna Vainshtein, Ao Zhang, Daniel R Zollinger, Yael Eshed-Eisenbach, Peter J Brophy, Matthew N Rasband, and Elior Peles. The paranodal cytoskeleton clusters na+ channels at nodes of ranvier. 6:e21392. ISSN 2050-084X. doi: 10.7554/eLife.21392.
56. Chuansheng Zhang, Keiichiro Susuki, Daniel R. Zollinger, Jeffrey L. Dupree, and Matthew N. Rasband. Membrane domain organization of myelinated axons requires βII spectrin. 203(3):437–443. ISSN 1540-8140, 0021-9525. doi: 10.1083/jcb.201308116.
57. Carmen Cifuentes-Diaz, Fabrice Chareyre, Marta Garcia, Jérôme Devaux, Michèle Carnaud, Grégoire Levasseur, Michiko Niwa-Kawakita, Sheila Harroch, Jean-Antoine Girault, Marco Giovannini, and Laurence Goutebroze. Protein 4.1b contributes to the organization of peripheral myelinated axons. 6(9):e25043, . ISSN 1932-6203. doi: 10.1371/journal.pone.0025043.
58. Steven Einheber, Xiaosong Meng, Marina Rubin, Isabel Lam, Narla Mohandas, Xiuli An, Peter Shrager, Joseph Kissil, Patrice Maurel, and James L. Salzer. The 4.1b cytoskeletal protein regulates the domain organization and sheath thickness of myelinated axons. 61 (2):240–253. ISSN 08941491. doi: 10.1002/glia.22430.
59. Veronica Brivio, Catherine Faivre-Sarrailh, Elior Peles, Diane L. Sherman, and Peter J. Brophy. Assembly of CNS nodes of ranvier in myelinated nerves is promoted by the axon cytoskeleton. 27(7):1068–1073. ISSN 09609822. doi: 10.1016/j.cub.2017.01.025.
60. Kathrin Doppler, Franziska Frank, Ann-Cathrin Koschker, Karlheinz Reiners, and Claudia Sommer. Nodes of ranvier in skin biopsies of patients with diabetes mellitus. 22(3):182–190, . ISSN 10859489. doi: 10.1111/jns.12224.
61. A A Sima, S A Lattimer, S Yagihashi, and D A Greene. Axo-glial dysjunction. a novel structural lesion that accounts for poorly reversible slowing of nerve conduction in the spontaneously diabetic bio-breeding rat. 77(2):474–484. ISSN 0021-9738. doi: 10.1172/JCI112326.
62. R. A. Malik, S. Tesfaye, P. G. Newrick, D. Walker, S. M. Rajbhandari, I. Siddique, A. K. Sharma, A. J. M. Boulton, R. H. M. King, P. K. Thomas, and J. D. Ward. Sural nerve pathology in diabetic patients with minimal but progressive neuropathy. 48(3):578–585. ISSN 0012-186X, 1432-0428. doi: 10.1007/s00125-004-1663-5.
63. Peter James Dyck, Alfred Lais, Jeannine L. Karnes, Peter O'Brien, and Robert Rizza. Fiber loss is primary and multifocal in sural nerves in diabetic polyneuropathy. 19(5):425–439, . ISSN 0364-5134, 1531-8249. doi: 10.1002/ana.410190503.
64. Tatyana M. Svitkina and Gary G. Borisy. [43] correlative light and electron microscopy of the cytoskeleton of cultured cells. In *Methods in Enzymology*, volume 298, pages 570–592. Elsevier. ISBN 978-0-12-182199-9. doi: 10.1016/S0076-6879(98)98045-4.
65. Tatyana Svitkina. Imaging cytoskeleton components by electron microscopy. In Ray H. Gavin, editor, *Cytoskeleton*, volume 2364, pages 25–52. Springer US. ISBN 978-1-07-161660-4 978-1-07-161661-1. doi: 10.1007/978-1-0716-1661-1_2. Series Title: Methods in Molecular Biology.
66. Marilyne Labasque, Bruno Hivert, Gisela Nogales-Gadea, Luis Querol, Isabel Illa, and Catherine Faivre-Sarrailh. Specific contactin n-glycans are implicated in neurofascin binding and autoimmune targeting in peripheral neuropathies. 289(11):7907–7918. ISSN 00219258. doi: 10.1074/jbc.M113.528489.
67. Constance Manso, Luis Querol, Mourad Mekaouche, Isabel Illa, and Jérôme J. Devaux. Contactin-1 IgG4 antibodies cause paranode dismantling and conduction defects. 139(6): 1700–1712, . ISSN 0006-8950, 1460-2156. doi: 10.1093/brain/aww062.
68. Constance Manso, Luis Querol, Cinta Lleixà, Mallory Poncelet, Mourad Mekaouche, Jean-Michel Vallat, Isabel Illa, and Jérôme J. Devaux. Anti–neurofascin-155 IgG4 antibodies prevent paranodal complex formation in vivo. 129(6):2222–2236, . ISSN 0021-9738, 1558-8238. doi: 10.1172/JCI124694.
69. Jean-Michel Vallat, Laurent Magy, Philippe Corcia, Jean-Marc Boulesteix, Antonino Uncini, and Stéphane Mathis. Ultrastructural lesions of nodo-paranodopathies in peripheral neuropathies. 79(3):247–255, . ISSN 0022-3069, 1554-6578. doi: 10.1093/jnen/nlz134.
70. Kathrin Doppler, Christian Werner, and Claudia Sommer. Disruption of nodal architecture in skin biopsies of patients with demyelinating neuropathies. 18(2):168–176, . ISSN 10859489. doi: 10.1111/jns5.12023.
71. Claudia Sommer. Nerve and skin biopsy in neuropathies. 31(5):534–540. ISSN 1350-7540, 1473-6551. doi: 10.1097/WCO.0000000000000601.
72. Kathrin Doppler, Christian Werner, Carsten Henneges, and Claudia Sommer. Analysis of myelinated fibers in human skin biopsies of patients with neuropathies. 259(9):1879–1887, . ISSN 0340-5354, 1432-1459. doi: 10.1007/s00415-012-6432-7.
73. Jean-Michel Vallat, Nobuhiro Yuki, Kenji Sekiguchi, Norito Kokubun, Nobuyuki Oka, Stéphane Mathis, Laurent Magy, Diane L. Sherman, Peter J. Brophy, and Jérôme J. Devaux. Paranodal lesions in chronic inflammatory demyelinating polyneuropathy associated with anti-neurofascin 155 antibodies. 27(3):290–293, . ISSN 09608966. doi: 10.1016/j.nmd.2016.10.008.
74. Haruki Koike, Masato Kadoya, Ken-ichi Kaida, Shohei Ikeda, Yuichi Kawagashira, Masahiro Iijima, Daisuke Kato, Hidenori Ogata, Ryo Yamasaki, Noriyuki Matsukawa, Jun-ichi Kira, Masahisa Katsuno, and Gen Sobue. Paranodal dissection in chronic inflammatory demyelinating polyneuropathy with anti-neurofascin-155 and anti-contactin-1 antibodies. 88(6):465–473. ISSN 0022-3050, 1468-330X. doi: 10.1136/jnnp-2016-314895.
75. Jean-Michel Vallat, Anne Vital, Laurent Magy, Marie-Laure Martin-Negrier, and Claude Vital. An update on nerve biopsy. 68(8):833–844, . ISSN 0022-3069, 1554-6578. doi: 10.1097/NEN.0b013e3181af2b9c.
76. Joachim Weis, Sebastian Brandner, Martin Lammens, Claudia Sommer, and Jean-Michel Vallat. Processing of nerve biopsies: A practical guide for neuropathologists. 31(1):7–23. ISSN 0722-5091. doi: 10.5414/NP300468.
77. P. J. Dyck, W. J. Johnson, E. H. Lambert, and P. C. O'Brien. Segmental demyelination secondary to axonal degeneration in uremic neuropathy. 46(6):400–431, . ISSN 0025-6196.
78. Min Xu, Marcus Pinto, Chenjing Sun, Janean K Engelstad, P James Dyck, Peter J Dyck, and Christopher J Klein. Expanded teased nerve fibre pathological conditions in disease association. 90(2):138–140, . ISSN 0022-3050, 1468-330X. doi: 10.1136/jnnp-2018-319077.
79. John W. Prineas. Demyelination and remyelination in recurrent idiopathic polyneuropathy: An electron microscope study. 18(1):34–57. ISSN 0001-6322, 1432-0533. doi: 10.1007/BF00684474.
80. Maria Nolano, Vincenzo Provitera, Claudio Crisci, Annamaria Stancanelli, Gwen Wendelschafer-Crabb, William Robert Kennedy, and Lucio Santoro. Quantification of myelinated endings and mechanoreceptors in human digital skin. 54(2):197–205. ISSN 0364-5134, 1531-8249. doi: 10.1002/ana.10615.
81. Kathrin Doppler, Luise Appeltshauser, Carmen Villmann, Corinna Martin, Elior Peles, Heidrun H. Krämer, Axel Haarmann, Mathias Buttmann, and Claudia Sommer. Autoantibodies to contactin-associated protein 1 (caspr) in two patients with painful inflammatory neuropathy. 139(10):2617–2630, . ISSN 0006-8950, 1460-2156. doi: 10.1093/brain/aww189.
82. Beate Hartmannsberger, Kathrin Doppler, Julia Stauber, Beate Schlotter-Weigel, Peter Young, Michael W Sereda, and Claudia Sommer. Intraepidermal nerve fibre density as biomarker in charcot–marie–tooth disease type 1a. 2(1):fcaa012. ISSN 2632-1297. doi: 10.1093/braincomms/fcaa012.
83. Ismail M. Khater, Ivan Robert Nabi, and Ghassan Hamarneh. A review of super-resolution single-molecule localization microscopy cluster analysis and quantification methods. 1(3): 100038. ISSN 26663899. doi: 10.1016/j.patter.2020.100038.
84. Aldo Zaimi, Maxime Wabartha, Victor Herman, Pierre-Louis Antonsanti, Christian S. Perone, and Julien Cohen-Adad. AxonDeepSeg: automatic axon and myelin segmentation from microscopy data using convolutional neural networks. 8(1):3816. ISSN 2045-2322. doi: 10.1038/s41598-018-22181-4.
85. Viktor Toth, Naveen Jayaprakash, Adam Abbas, Ariba Khan, Stavros Zanos, and Theodoros P. Zanos. Single-axon level automatic segmentation and feature extraction from immuhistochemical images of peripheral nerves. In *2020 42nd Annual International Conference of the IEEE Engineering in Medicine & Biology Society (EMBC)*, pages 1859–1862. IEEE. ISBN 978-1-72811-990-8. doi: 10.1109/EMBC44109.2020.9175974.
86. De-En Xu, Wen-Min Zhang, Zara Zhuyun Yang, Hong-Mei Zhu, Ke Yan, Shao Li, Dominique Bagnard, Gavin S Dawe, Quan-Hong Ma, and Zhi-Cheng Xiao. Amyloid precursor protein at node of ranvier modulates nodal formation. 8(4):396–403, . ISSN 1933-6918, 1933-6926. doi: 10.4161/cam.28802.
87. Iván Coto Hernández, Suresh Mohan, Steven Minderler, and Nate Jowett. Super-resolved fluorescence imaging of peripheral nerve. 12(1):12450. ISSN 2045-2322. doi: 10.1038/s41598-022-16769-0.
88. J. Michael Schröder. Developmental and pathological changes at the node and paranode in human sural nerves. 34(5):422–435. ISSN 1059-910X, 1097-0029. doi: 10.1002/(SICI)1097-0029(19960801)34:5<422::AID-JEMT2>3.0.CO;2-O.
89. Claudia Schwab, Vimala Bondada, D. Larry Sparks, Leslie D. Cahan, and James W. Geddes. Postmortem changes in the levels and localization of microtubule-associated proteins (tau, MAP2 and MAP1b) in the rat and human hippocampus. 4(2):210–225. ISSN 1050-9631, 1098-1063. doi: 10.1002/hipo.450040212.
90. G. Wolswijk. Changes in the expression and localization of the paranodal protein caspr on axons in chronic multiple sclerosis. 126(7):1638–1649. ISSN 1460-2156. doi: 10.1093/brain/awg151.
91. Z. Cai, J.W. Finnie, P.C. Blumbergs, J. Manavis, M.N. Ghabriel, and P.D. Thompson. Early paranodal myelin swellings (tomacula) in an avian riboflavin deficiency model of demyelinating neuropathy. 198(1):65–71. ISSN 00144886. doi: 10.1016/j.expneurol.2005.10.028.
92. ICMJE | recommendations | defining the role of authors and contributors.
93. Arturo Casadevall, Gregg L. Semenza, Sarah Jackson, Gordon Tomaselli, and Rexford S.

Ahima. Reducing bias: accounting for the order of co–first authors. 129(6):2167–2168. ISSN 0021-9738, 1558-8238. doi: 10.1172/JCI128764.
94. Peter Y. K. Van den Bergh, Pieter A. Doorn, Robert D. M. Hadden, Bert Avau, Patrik Vankrunkelsven, Jeffrey A. Allen, Shahram Attarian, Patricia H. Blomkwist-Markens, David R. Cornblath, Filip Eftimov, H. Stephan Goedee, Thomas Harbo, Satoshi Kuwabara, Richard A. Lewis, Michael P. Lunn, Eduardo Nobile-Orazio, Luis Querol, Yusuf A. Rajabally, Claudia Sommer, and Haluk A. Topaloglu. European academy of neurology/peripheral nerve society guideline on diagnosis and treatment of chronic inflammatory demyelinating polyradiculoneuropathy: Report of a joint task force—second revision. 26(3):242–268. ISSN 1085-9489, 1529-8027. doi: 10.1111/jns.12455.
95. Angela Dispenzieri. POEMS syndrome: 2017 update on diagnosis, risk stratification, and management: DISPENZIERI. 92(8):814–829. ISSN 03618609. doi: 10.1002/ajh.24802.
96. Michael P. Collins, P. James B. Dyck, Gary S. Gronseth, Loïc Guillevin, Robert D. M. Hadden, Dieter Heuss, Jean-Marc Léger, N.C. Notermans, John D. Pollard, Gérard Said, Gen Sobue, A.F.J.E. Vrancken, and John T. Kissel. Peripheral nerve society guideline* on the classification, diagnosis, investigation, and immunosuppressive therapy of non-systemic vasculitic neuropathy: executive summary. 15(3):176–184. ISSN 10859489. doi: 10.1111/j.1529-8027.2010.00281.x.
97. I S J Merkies. Clinimetric evaluation of a new overall disability scale in immune mediated polyneuropathies. 72(5):596–601. ISSN 00223050. doi: 10.1136/jnnp.72.5.596.
98. Ruud P. Kleyweg, Frans G. A. Van Der Meché, and Paul I. M. Schmitz. Interobserver agreement in the assessment of muscle strength and functional abilities in guillain-barré syndrome: Muscle strength assessment in GBS. 14(11):1103–1109. ISSN 0148639X. doi: 10.1002/mus.880141111.
99. Johannes Schindelin, Ignacio Arganda-Carreras, Erwin Frise, Verena Kaynig, Mark Longair, Tobias Pietzsch, Stephan Preibisch, Curtis Rueden, Stephan Saalfeld, Benjamin Schmid, Jean-Yves Tinevez, Daniel James White, Volker Hartenstein, Kevin Eliceiri, Pavel Tomancak, and Albert Cardona. Fiji: an open-source platform for biological-image analysis. 9(7):676–682. ISSN 1548-7091, 1548-7105. doi: 10.1038/nmeth.2019.
100. M.D. Abramoff, Paulo J. Magalhães, and Sunanda J. Ram. Image processing with ImageJ. 11(7):36–42. ISSN 1081-8693.
101. Kathrin Doppler, Luise Appeltshauser, Heidrun H. Krämer, Judy King Man Ng, Edgar Meinl, Carmen Villmann, Peter Brophy, Sulayman D. Dib-Hajj, Stephen G. Waxman, Andreas Weishaupt, and Claudia Sommer. Contactin-1 and neurofascin-155/-186 are not targets of auto-antibodies in multifocal motor neuropathy. 10(7):e0134274, . ISSN 1932-6203. doi: 10.1371/journal.pone.0134274.
102. Varun Venkataramani, Frank Herrmannsdörfer, Mike Heilemann, and Thomas Kuner. SuReSim: simulating localization microscopy experiments from ground truth models. 13 (4):319–321. ISSN 1548-7091, 1548-7105. doi: 10.1038/nmeth.3775.
103. Martin Ovesný, Pavel Křížek, Josef Borkovec, Zdeněk Švindrych, and Guy M. Hagen. ThunderSTORM: a comprehensive ImageJ plug-in for PALM and STORM data analysis and super-resolution imaging. 30(16):2389–2390. ISSN 1367-4803, 1460-2059. doi: 10.1093/bioinformatics/btu202.
104. Ignacio Arganda-Carreras, Carlos O. S. Sorzano, Roberto Marabini, José María Carazo, Carlos Ortiz-de Solorzano, and Jan Kybic. Consistent and elastic registration of histological sections using vector-spline regularization. In Reinhard R. Beichel and Milan Sonka, editors, *Computer Vision Approaches to Medical Image Analysis*, volume 4241, pages 85–95. Springer Berlin Heidelberg. ISBN 978-3-540-46257-6 978-3-540-46258-3. doi: 10.1007/11889762_8. Series Title: Lecture Notes in Computer Science.
105. Dirk Padfield. Generalized normalized cross correlation.
106. Barbara Zonta, Steven Tait, Shona Melrose, Heather Anderson, Sheila Harroch, Jennifer Higginson, Diane L. Sherman, and Peter J. Brophy. Glial and neuronal isoforms of neurofascin have distinct roles in the assembly of nodes of ranvier in the central nervous system. 181(7):1169–1177. ISSN 1540-8140, 0021-9525. doi: 10.1083/jcb.200712154.
107. Perrine Charles, Steven Tait, Catherine Faivre-Sarrailh, Gilles Barbin, Frank Gunn-Moore, Natalia Denisenko-Nehrbass, Anne-Marie Guennoc, Jean-Antoine Girault, Peter J. Brophy, and Catherine Lubetzki. Neurofascin is a glial receptor for the paranodin/caspr-contactin axonal complex at the axoglial junction. 12(3):217–220. ISSN 09609822. doi: 10.1016/S0960-9822(01)00680-7.

Online Methods

Patients, clinical and histopathological diagnosis. We prospectively included n = 17 patients with peripheral neuropathies who had undergone a sensory nerve biopsy during the routine diagnostic workup process at the University hospital of Würzburg between July 2018 and April 2021. Demographic and clinical data including laboratory results, nerve conduction studies and suspected clinical diagnosis were assessed retrospectively from the patients' records. HbA1c values were assessed at the time point of the nerve biopsy and diabetes mellitus was classified according to WHO criteria. Diagnostic criteria for chronic inflammatory demyelinating polyradiculoneuropathy (CIDP) (94), POEMS syndrome (95) and vasculitic neuropathy (96) were assessed in patients with the respective clinical diagnosis. Clinical disease severity respective to motor function was assessed retrospectively by applying standardized clinical scores: The Overall disability sum Score (ODSS) (97) and the Medical Research Council (MRC) Sum Score for levels of paresis (98). Clinical data of individual patients are shown in Supplemental Table S1). The histopathological diagnosis was assessed in each biopsy by a trained and blinded researcher reevaluating the routine staining including semithin sections with toluidine blue staining, cryosection including H&E staining and immunohistochemistry for T-cell marker anti-Leu4 and paraffin-embedded sections including H&E, congo red and Elastica van Gieson staining and immunohistochemistry for macrophages using anti-CD68 and lymphocytes using anti-CD8 according to standard protocols as previously described (40). Onion bulb structures, regeneration clusters, thinly myelinated fibers and Wallerian degeneration were counted per fascicle in each patient. Axonal loss was quantified in a semi-quantitative manner (mild, moderate, severe) and large fibers per fascicle were counted and the area of the fascicle was measured using FIJI (99, 100) to calculate the fiber density (unit: fibers/mm^2).

Teased fiber preparation. Murine teased fibers we prepared as previously described (101). In brief, adult C57/Bl6 mice were sacrificed by cervical dislocation. Sciatic nerve and sural nerve were dissected, fixed for 10 minutes in 4% PFA, and washed in 1M phosphate buffer. Human sensory nerve preparations (n = 16 sural nerve, n = 1 superficial radial nerve) were obtained from leftovers of routine nerve biopsy during the routine diagnostic workup process on patients with polyneuropathies of unknown etiology at the University Hospital of Würzburg. Remaining material was cut into 5-mm slices with a scalpel and fixed and washed as described above. Teasing was performed in 0.5 M phosphate buffer. Epineural connective tissue and the perineurium was removed with fine forceps. The remaining nerve fascicle was used for teased fiber preparation, including endoneurial connective tissue, so that teased fiber preparations of samples with loss of nerve fibers contained a lower number of fibers.For *d*STORM microscopy, the fibers were teased on ultra-cleaned, PDL-coated 24-mm glass coverslips. For confocal microscopy, the fibers were teased on Airyscan Superfrost Slides. Slides and coverslips were dried overnight and stored at -20°C until use. The teasing process was performed by a technician or investigator and two or less attempts on learning the teasing process resulted in sufficient results. The whole procedure of human sural nerve fixation, preparation and teasing took a maximum of 60 minutes or less.

Simulated Datasets. Simulations of super-resolution microscopy datasets were performed with the SuReSim software package (102). The periodic ground truth structure is available on Zenodo (see data sharing statement) and the simulation parameters are summarized in Supplemental Table S6). The localization text-files were transformed into ThunderSTORM (103) compatible csv-files and super-resolution images with a custom MatLab script. Simulated datasets were analyzed the same way as the experimental datasets (see below).

Immunostaining for *d*STORM and confocal microscopy. The thawed teased fibers were fixed for 20 minutes in 100% Acetone at -20 °C. After washing with Phosphate-buffered saline (PBS) and permeabilization with 2% Triton-X for 30 min, they were blocked in PBS containing 1mg/ml Biotin-BSA, 4% BSA and 0,5% Triton-X for 60 min. Dual-color immunolabeling was performed by overnight incubation at + 4 °C with the primary antibody diluted in PBS with 0.5% Triton-X and 1% BSA (see Supplemental Table S7). For *d*STORM imaging, fiducial markers were immobilized on the surface by an additional 20 min incubation step with 0.1 mg/ml Neutravidin (Thermo Scientific™, 31000) and three PBS washing steps right before the initiation of the secondary antibody incubation. During the secondary antibody incubation 35 pM biotinylated gold nanorods (Nanopartz C12-25-650-TB) were added. After secondary antibody incubation for 1h at room temperature, slides and coverslips were washed and *d*STORM coverslips were stored PBS. For Airyscan imaging, the slides were embedded in Vectashield antifade mounting medium (Vector laboratories, VEC-H-1000).

***d*STORM Fluorescence image acquisition.** Dual-color *d*STORM microscopy was performed with an inverted light microscope (Zeiss Observer Z.1, Carl Zeiss AG) customized for SMLM (Supplemental Table S8). The *d*STORM blinking buffer contained 100 mM MEA (Sigma, M6500), 20 mM D-glucose (Sigma, G7528), 0.55 mg ml-1 gluco-oxidase (Roth, 60281), 0.011 mg ml-1 catalase (Sigma, C1345) in PBS. The pH was adjusted to pH 7.9 with 5M KOH (Sigma, 30603). After applying the *d*STORM buffer, imaging was performed with the acquisition parameters summarized in Supplemental Table S9. For color channel alignment, calibration images with 100 nm TetraSpeck microspheres (ThermoFisher, T7279) immobilized on glass coverslips were recorded simultaneously in both channels.

***d*STORM image reconstruction.** *d*STORM images were reconstructed with the ImageJ plugin ThunderSTORM (103) as specified in Supplemental Table S9). Based on the filtered localization data, a super-resolved image with a pixel size of 10.6 nm was reconstructed by Gaussian rendering or as a scatter plot. For the channel alignment, the TetraSpeck images were localized and a super-resolved image with a pixel size of 10.6 nm was reconstructed for each channel. Based on these calibration images, a transformation matrix of the A532 channel onto the A647 was calculated with the ImageJ plugin bunwarpJ (104). This transformation matrix was directly applied to the reconstructed super-resolved images or to the localization data itself with a MatLab script.

***d*STORM image autocorrelation analysis.** The image autocorrelation analysis was performed based on the localization data with a MatLab routine (Scripts and manuals are available on Zenodo, see Data sharing statement). With the routine, several regions of interest (ROIs) within the paranodal and internodal region were selected manually in the super-resolved reconstruction of the respective node (width = 600 nm; lengths along the axon were manually chosen by selecting a start and end point of the centerline). Based on localization data contained in each ROI, a super-resolved image was reconstructed after rotating the ROI to align the image along the x-axis. The rotation angle was varied within a ± 20° range by 1°- steps to align the repetitive line structure perpendicularly to the x-axis. The resulting reconstructed images were autocorrelated in 2D with the Normxcorr2_general.m function (105). The optimal rotation angle was selected based on a maximizing of the autocorrelation along the center y-axis. MatLab output correlation images (pixelsize 2 nm) were analyzed in FIJI with line plots averaged over a width of 150 pixels. Plots were imported into OriginPro (Origin2021b, OriginLab Corp.). Gauss distribution curves were fitted and the peak to peak distances of those distribution curves were calculated.

***d*STORM image colocalization analysis.** To estimate the image resolution the raw time series image stacks were split into even and colocalization analysis on transformed dual-color *d*STORM datasets was performed with a tessellation-based approach (30). Paranodal regions were defined by Caspr-1 staining, each representing a region of interest. Herewithin, Manders' A & B correlation coefficients of all channels were calculated to assess colocalization (38, 39). The pan-neurofascin antibody used in this study stained both glial neurofascin-155 isoform at the paranode and neuronal neurofascin-186 isoform at the node, which have different localizations and functions (41, 106, 107). In this study, we exclusively studied neurofascin-155 and its interaction with Caspr-1, therefore we exclusively studied the paranodal region. The nodal region within the pan-neurofascin staining was not considered in the analysis. The colocalization data was analyzed using OriginPro (Origin2021b, OriginLab Corp.).

Large field of view confocal imaging and assessment. High-content 3D three-color confocal microscopy at a 20-fold magnification including stacks and tiles was performed with a Zeiss LSM 980 Airyscan 2 (Carl Zeiss AG) using Zen blue 3.3 software (Carl Zeiss AG) for Airyscan 3D processing and stitching of tiles. Acquisition and image processing parameters are listed in Supplemental Table S9. The total tissue volume in high-content images was calculated with either a custom FIJI script (available on Zenodo, see data sharing statement) or via Imaris image segmentation (Oxford Instruments, v9.9.0). In both cases, total tissue volume calculation was based on unspecific background binding of the pan-neurofascin antibody, as this was the most pronounced. As for the FIJI script, images were filtered with a 3d gaussian blur and then classified into "tissue" and "non tissue" by a low static threshold. In Imaris, images were segmented with an image smoothing of 1µm, an intensity threshold set to individual values in every image ranging from 30 till 200 (16 bit images) and resulting objects were filtered for volume (voxel) greater than 10000. To count and locate nodes of Ranvier automatically, specific anti-pan-neurofascin staining was segmented in Imaris. Imaging smoothing was set

to 2 times pixelsize (0.15 µm) and intensity threshold was set manually to values (500-1400) including stained nodes of Ranvier individually for every image. Last resulting objects were filtered by volume (voxel) and all accidentally false detected Schmidt-Lanterman incisures were discarded. Automated analysis was performed in n = 20 high-content images of murine sciatic nerves and n = 20 high-content images from human samples. For comparison and accuracy assessment, the number of nodes per sample was counted using FIJI by two independent blinded investigators, assessing the whole slide. Morphometrics of the nodes of Ranvier were assessed and compared via two methods: Firstly, automatically assessed nodo-paranodal length was calculated from Imaris ellipsoid axes of pan-neurofascin staining in n = 20 slides of murine and human samples (see above and Supplemental Figure S3). Secondly, morphometrics were assessed on the same slides in a blinded manner by FIJI defining linear ROIs as indicated in Figure 4: nodo-paranodal length was defined as the maximal extension of both Caspr-1 blocks and the nodal gap in between; the nodal gap was defined as the smallest gap between two paranodal Caspr-1 blocks; the paranodal diameter was defined as the maximal diameter of paranodal Caspr-1 staining. Accuracy of automated assessment of nodo-paranodal length using Imaris did not reach as exact results as manual measurement (see Supplemental Figure S3). Therefore, blinded manual assessment was performed on all samples. For assessment of nodo-paranodal morphometrics in patients, n = 40 randomly selected nodes of Ranvier were measured in each patient sample of n = 9 patients. In n = 7 patients, the maximal number of nodes per field of view was < 40 nodes, so all visible nodes within the field of view were assessed (n = 22 - 39 nodes, see Supplemental Table S5).

Statistics. We assessed statistical significance with OriginPro Version 2021b SR2 9.8.5.212 (OriginLab Corp.) and Prism V9.3.0 (GraphPad Software, San Diego, CA). Testing for normality distribution was performed using d'Agostino Pearson test and Shapiro-Wilk test. The further specific tests used in the analysis are described in the respective figure and table legends. Results with p-values less than 0.05 were considered significant.

Super-resolution imaging pinpoints ultrastructural changes at the node of Ranvier in patients with polyneuropathy

Appeltshauser, Linke Heil et al., 2022

Supplementary Material

Supplementary Tables 1-9.

Supplementary Figures 1-3.

Supplementary Bibliography.

no	age	sex	clinical presentation	NCS classification	SNAP (μV)	SNAP (% of LLN)	disease duration (months)	diabetes mellitus	HbA1c	CSF (cells; total protein in mg/l)	suspected etiology	diagnostic criteria (EAN/PNS (1, 2))
1	21-30	male	distal asymmetric sensorimotor	axonal	4.7	47	18	no	5.3	n/a	vasculitic	pathologically definite vasculitic neuropathy(1)
2	61-70	male	distal asymmetric sensorimotor	axonal	7.0	70	12	no	6.0	1/497	vasculitic	clinically probable vasculitic neuropathy(1)
3	81-90	male	distal symmetric sensorimotor	axonal	0.0	0	2	no	6.5	n/a	vasculitic	pathologically definite vasculitic neuropathy(1)
4	51-60	male	distal asymmetric sensorimotor	axonal	0.0	0	7	no	5.1	2/404	vasculitic	clinically probable vasculitic neuropathy(1)
5	61-70	male	distal asymmetric sensorimotor	axonal	1.8	36	1	no	5.8	1/396	vasculitic	clinically probable vasculitic neuropathy(1)
6	71-80	female	distal symmetric sensorimotor	axonal	0.0	0	5	yes	6.3	3/1070	POEMS	POEMS(3)
7	51-60	female	distal asymmetric sensorimotor	axonal	2.1	70	15	yes	6.5	3/606	vasculitic	clinically probable vasculitic neuropathy(1)
8	71-80	male	distal symmetric sensorimotor	axonal	0.0	0	1	no	5.5	3/796	vasculitic	clinically probable vasculitic neuropathy(1)
9	31-40	male	distal symmetric sensorimotor	demyelinating	7.7	77	96	no	5.9	3/333	unknown/ vitamin B12 deficiency	n/a
10	61-70	female	distal symmtric sensorimotor	axonal	2.7	54	20	no	5.7	1/454	unknown	n/a
11	61-70	male	proximal asymmetric sensorimotor	axonal	1.9	38	55	no	5.7	4/407	unknown	n/a
12	51-60	male	distal symmetric sensorimotor	demyelinating	10.5	100	4	no	4.9	28/2700	CIDP variant	CIDP(2)
13	51-60	male	distal symmetric sensorimotor	mixed	2.9	29	26	no	5.0	2/586	CIDP	possible CIDP(2)
14	31-40	male	distal symmetric sensorimotor	demyelinating	3.4	34	264	no	5.1	4/1940	CIDP	CIDP(2)
15	61-70	male	distal asymmetric sensorimotor	mixed	5.2	52	69	no	5.4	5/618	CIDP variant	possible CIDP(2)
16	51-60	female	distal asymmetric sensorimotor	axonal	7.0	70	21	no	n/a	2/211	CIDP variant	possible CIDP(2)
17	61-70	male	distal symmetric sensorimotor	axonal	0.0	0	243	no	5.3	1/599	hereditary	n/a

Table S1. Demographic data and clinical of the cohort of patients with polyneuropathy. Abbreviations: CIDP = chronic inflammatory demyelinating polyradiculoneuropathy, CSF = cerebrospinal fluid, n/a = not applicable or not assessed, LLN = lower limit of normal, NCS = nerve conduction studies, no = number, POEMS = polyneuropathy, organomegaly, endocrinopathy, myeloma protein, and skin changes (osteosclerotic myeloma), SNAP = Sensory nerve action potential.

no	onion bulbs	regenerating clusters	thinly myelinated fibers	Wallerian degeneration	large fibers	fascicle area (μm^2)	fiber density (large fibers/mm^2)	mean fiber density	signs of inflammation/vessel pathology	severity axonal loss	acuteness	type
1	0/0	0/0	2/2	2/1	297/129	131469/114096	2259/1131	1695	perivascular leukocytes (including the vessel wall), fragmentation of lamina elastica interna, necrosis	moderate	acute	axonal
2	0/0	2/1	3/0	4/5	222/132	118621/68965	1872/1914	1893	perivascular leukocytes (including the vessel wall)	moderate	acute	axonal
3	0/0	0/2	0/0	16/6	50/141	130332/117842	384/1197	790	perivascular leukocytes (including the vessel wall), fragmentation of internal elastic lamina	moderate	acute	axonal
4	0/0	2/0	0/0	9/6	10/11	114664 / 98878	87 / 111	99	perivascular leukocytes (including the vessel wall), endoneural macrophages	severe	acute	axonal
5	0/0	0/0	0/0	32/42	32/42	103204/72460	230/745	488	perivascular leukocytes (including the vessel wall), endoneural macrophages	severe	acute	axonal
6	0/0	4/0	4/2	3/11	38/29	105348/54121	361/546	453	perivascular leukocytes	severe	acute	axonal
7	0/0	2/2	3/1	0/2	67/410	57923/107453	1157/3816	2486	perivascular leukocytes, endoneural macrophages	mild	chronic	axonal
8	5/1	9/6	4/1	0/0	71/161	58634/103384	1211/1557	1384	perivascular leukocytes, fragmentation of elastic lamina	moderate	chronic	axonal
9	3/3	3/2	3/3	0/0	121/98	113839/55362	1063/1770	1417	none	moderate	chronic	axonal
10	0/0	7/5	18/12	0/0	185/143	85716/51282	2158/2788	2473	none	moderate	chronic	axonal
11	0/0	3/4	4/2	3/3	191/134	62462/42427	3058/3158	3108	endoneural macrophages	mild	chronic	axonal
12	3/0	8/5	5/2	0/0	552/218	104192/75243	5298/2897	4098	perineural leukocytes	mild	chronic	axonal
13	5/0	2/0	35/3	2/1	98/24	66966/19482	1463/1232	1348	perivascular leukocytes, perivascular and endoneural macrophages	severe	chronic	demyelinating
14	3/6	7/6	18/3	0/0	205/196	104881/115955	1955/1690	1822	endoneural and perivascular leukocytes, endoneural macrophages	moderate	chronic	demyelinating
15	2/1	4/6	29/41	0/1	125/142	52967/194474	2360/1359	1860	none	moderate	chronic	demyelinating
16	2/2	0/1	12/7	0/1	215/155	87379/54731	2461/2832	2646	endoneural and perivascular macrophages	mild	chronic	demyelinating
17	2	6/2	24/6	0/0	110/95	78121/55787	1408/1703	1555	none	moderate	chronic	demyelinating

Table S2. Histopathologic parameters and classification of patients with polyneuropathy. In each patient, semithin cross sections of sensory nerve biopsy (patient 7: superficial radial nerve, other patients: sural nerve) with toluidine blue staining were evaluated for histopathological classification. Total counts of onion bulb figures, thinly myelinated fibers, Wallerian degeneration and large fibers are displayed for two fascicles per patient. Fascicle area was measured using FIJI. Fiber density was calculated as n(large fibers) / mm^3 and is displayed both for the single fascicles and as the mean fiber density. Furthermore, immunostainings were evaluated as described in the methods to check for signs of inflammation and amyloid deposition, and if positive, are reported above. Histopathologic classification including semiquantitative assessment of axonal loss, acuteness of disease and type (axonal or demyelinating) was performed by a trained and blinded researcher. Abbreviations: no = number.

3A) type	**axonal** (n=12)	**demyelinating** (n=5)	**p-value**
median count of onion bulbs/fascicle	0	2	0.0047
median count of thinly myelinated fibers/fascicle	2.3	15	0.0015
3B) acuteness	**acute** (n=6)	**chronic** (n=12)	**p-value**
median Wallerian degeneration figures/fascicle	7.3	0.0	0.0003
median count of regenerating clusters / fascicle	1.0	4.0	0.0076
median disease duration (months)	6	42	0.021

3C) severity	**mild** (n=4)	**moderate** (n=8)	**sever** (n=4)	**p-value**
mean large fiber density (1/mm^2)	3085 ± 725	1654 ± 459	597 ± 531	$p_{mild\,vs.\,sever} < 0.0001$ $p_{moderate\,vs.\,sever} = 0.0176$
SNAP (% of LLN)	69.6 ± 25.32	37.11 ± 30.54	16.25 ± 18.98	$p_{mild\,vs.\,sever} < 0.04$ $p_{moderate\,vs.\,sever} = 0.4$

Table S3. Histopathological and clinical differences between groups of histopathological classification. For histopathological classification, patients were classified into histopathological 3A) type (axonal and demyelinating neuropathy) by counting signs of demyelination such as onion bulb figures and thinly myelinated fibers/fascicle. Furthermore, 3B) histopathological acuity was determined by counting signs of de- and regeneration and correlated to clinical disease duration. 3C) histopathological severity was rated semi-quantitatively in mild, moderate and severe and assessed quantitatively by counting the large fiber density/mm^2. Electrophysiological parameters (SNAP) were assessed and compared in the three histopathological severity groups. The last column shows results of statistical testing between the groups using Kruskal-Wallis test with Dunn's correction for multiple testing if necessary (adjusted p-values are shown). Abbreviations: LLN = lower limit of normal, SNAP = Sensory nerve action potential.

4 A) autocorrelation peak-to peak distance (periodicity)

protein	localization	mouse	human		p-value
			axonal	demyelinating	
ß2-spectrin	internode	187.54 ± 20.59	183.97 ± 12.96		0.18
			183.05 ± 13.87	187.72 ± 7.94	
			p = 0.89	p = 0.74	
ß2-spectrin	paranode	184.28± 16.04	197.35 ± 36.18		0.03
			201.81 ± 41.38	190.66 ± 27.46	
			p = 0.006	p = 1	
Caspr-1	paranode	186.63 ± 24.73	247.15 ± 98.668		< 0.0001
			256.16 ± 100.11	203.25 ± 78.73	
			p < 0.00001	p < 0.00001	
Pan-NF	paranode	173.16 ± 23.61	283.85 ± 124.63		< 0.0001
			283.27 ± 125.94	293.36 ± 106.13	
			p = p < 0.00001	p < 0.00001	

4 B) colocalization (Manders' A correlation coefficients)

protein 1	protein 2	mouse	human			p-value
			acute axonal	chronic axonal	demyelinating	
Caspr-1	ß2-spectrin	0.91 ± 0.05		0.76 ± 0.15		< 0.0001
			0.73 ± 0.18	0.79 ± 0.12	0.79 ± 0.13	
			p < 0.0001	p = 0.003	p = 0.002	
Caspr-1	neurofascin-155 (paranode)	0.90 ± 0.06		0.87 ± 0.07		0.93
			0.88 ± 0.06	0.87 ± 0.06	0.87 ± 0.1	
			p < 0.0001	p = 0.003	p = 0.002	

4 C) colocalization (Manders' B correlation coefficients)

protein 1	protein 2	mouse	human			p-value
			acute axonal	chronic axonal	demyelinating	
Caspr-1	ß2-spectrin	0.75 ± 0.18		0.55 ± 0.21		< 0.001
			0.48 ± 0.23	0.70 ± 0.17	0.53 ± 0.14	
			p < 0.0001	p = 1	p = 0.006	
Caspr-1	neurofascin-155 (paranode)	0.88 ± 0.07		0.84 ± 0.09		0.25
			0.84 ± 0.07	0.85 ± 0.07	0.82 ± 0.13	
			p < 0.52	p = 1	p = 0.72	

Table S4. *d*STORM imaging parameters in mice and patients with polyneuropathies.(A) Autocorrelation peak-to peak distances (periodicity) of internodal and paranodal ß2-spectrin, Caspr-1 and neurofascin-155 in mice and patients with polyneuropathies. (B-C): Colocalization analysis using Manders' A and B correlation coefficients between Caspr-1 with ß2-spectrin and with the paranodal fraction of pan-neurofascin (neurofascin-155) are displayed in mouse and human Nodes of Ranvier. P-values of Kruskal-Wallis test with Dunn's correction for multiple testing are shown in the right column (mouse vs. human) and below the individual results of subanalysis (mouse vs. human axonal / demyelinating neuropathy subcohort).

no	n of measured nodes	nodal count	axonal paranodal diameter			nodo-paranodal length			nodal length		
		nodes/tissue volume (mm^3)	mean ± SD (µm)	median (µm)	adjusted p-value	mean ± SD (µm)	median (µm)	adjusted p-value	mean ± SD (µm)	median (µm)	adjusted p-value
1	40	16.91	2.74 ± 1.12	2.57	0.1072	13.09 ± 5.51	11.45	0.0006	1.17 ± 1.58	0.89	>0.9999
2*	40	21.53	2.85 ± 0.75	2.85	0.0004	14.11 ± 6.45	12.30	<0.0001	0.99 ± 0.81	0.79	>0.9999
3	40	18.32	2.16 ± 0.65	2.23	>0.9999	13.88 ± 7.74	10.40	0.0016	1.16 ± 0.33	1.10	0.1692
4	26	12.17	2.40 ± 0.96	2.46	>0.9999	12.21 ± 2.91	11.26	0.0032	0.91 ± 0.60	0.84	>0.9999
5	39	14.17	1.80 ± 0.66	1.64	0.1171	14.36 ± 6.66	12.25	<0.0001	1.23 ± 0.81	1.06	0.5359
6	37	13.22	2.08 ± 0.73	1.93	>0.9999	24.66 ± 17.64	15.99	<0.0001	2.16 ± 2.49	1.45	<0.0001
7	40	38.96	2.41 ± 0.95	2.26	>0.9999	12.99 ± 9.33	9.88	0.3935	1.73 ± 3.96	0.86	>0.9999
8*	40	30.12	2.16 ± 0.84	1.94	>0.9999	12.11 ± 6.11	10.65	0.0487	0.81 ± 0.49	0.70	>0.9999
9	22	18.28	2.61 ± 1.01	2.32	>0.9999	16.43 ± 10.16	13.16	0.0002	1.07 ± 0.83	0.78	>0.9999
10	38	28.67	2.26 ± 0.93	2.01	>0.9999	10.90 ± 3.35	10.74	0.2976	0.85 ± 0.34	0.78	>0.9999
11	40	36.37	2.03 ± 0.65	1.95	>0.9999	13.65 ± 8.22	11.53	0.0012	0.92 ± 1.59	0.59	0.2211
12*	40	47.41	1.79 ± 0.72	1.48	0.0652	11.29 ± 3.23	10.56	0.1324	0.92 ± 0.74	1.48	<0.0001
13	35	22.31	2.39 ± 0.93	2.23	>0.9999	14.96 ± 2.39	11.79	<0.0001	0.93 ± 0.59	0.76	>0.9999
14*	40	19.95	2.74 ± 1.14	2.57	0.334	10.46 ± 7.81	9.47	>0.9999	0.93 ± 0.93	0.71	>0.9999
15	40	21.80	3.14 ± 1.11	3.21	0.0001	11.49 ± 3.08	10.73	0.0231	1.32 ± 0.40	1.27	0.0008
16	30	82.68	2.86 ± 1.12	2.89	0.0651	14.00 ± 6.67	11.53	0.0008	1.16 ± 1.75	0.65	>0.9999
17	235	32.51	2.24 ± 0.58	2.20	>0.9999	14.35 ± 8.26	12.80	<0,0001	1.23 ± 0.52	1.16	0.0727

Table S5. Morpometics at the Node: High content confocal imaging and analysis data in single patients. Means ± standard deviations and medians of nodo-paranodal parameters (nodes / tissue volume, axonal paranodal diameter, nodo-paranodal length, nodal length) are shown for single patients of the cohort. Adjusted p-values are displayed compared to intact human nerves using Kruskal-Wallis test with Dunn's correction for multiple testing. Patient biopsies that were used to select intact nodes are marked with asterisks. Abbreviations: no = number, SD standard deviation.

Parameter [unit]	Values
angle of antibodies [degree]:	90.00
sigma of antibodies deviation [degree]:	0.00
binding sites per nm [nm^{-1}]:	0.05
labeling efficiency [%]:	10, 25, 50, 75, 100
radius of filament [nm]:	12.5
fluorophores per label:	2.0
label epitope distance [nm]:	20.0
localization precision (sigma x,y) [nm]:	20.0
localization precision (sigma z) [nm]:	70.0
binding sites per square nanometer [nm^{-2}]:	0.016666668
frames:	20000
duty cycle:	5.0E-4
bleaching constant [1/10000 frames]:	2.231E-5
median photon number:	4000
detection efficiency [%]:	50.0
background events per volume [$1/m^3$]:	25, 50, 75, 100
FWHM of PSF [nm]:	647.0
pixel size for output images in nm:	10.0

Table S6. Summary of the parameters for the simulation of SMLM datasets of ground truth periodic line patterns with SuReSim. The parameter sets used in the sweep are highlighted in gray.

target protein (conjugate)	host	dilution	company	catalogue number
pan-neurofascin	polyclonal chicken IgY	0.4 µg/ml	R & D Systems	AF3235
Caspr-1	polyclonal rabbit IgG	0.2 µg/ml	Abcam	ab34151
b2-Spectrin II	monoclonal mouse IgG	5 µg/ml	BD Biosciences	612563
Myelin basic protein	monoclonal rat IgG	10 µg/ml	Abcam	ab7349
chicken IgY(Alexa 647)	polyclonal goat IgG	10 µg/ml	Invitrogen	A-21449
rabbit IgG (Alexa532)	polyclonal goat IgG	10 µg/ml	Invitrogen	A-11009
rat IgG (Alexa488)	polyclonal donkey IgG	3.75 µg/ml	Jackson IR	712-545-150
rabbit IgG (Cy3)	polyclonal donkey IgG	5 µg/ml	Jackson IR	711-165-152

Table S7. Antibodies used for fluorescence stainings

Illumination	640 nm laser (iBEAM-smart-640-S, Toptica) 532 nm laser (GEM 532 nm, 250 mW, Laser Quantum)
Clean up filters	640/8 nm MaxDiode™ laser clean-up, Semrock Filter ZET 532/10 clean-up, Chroma
Dichroic filter	QuadLine Laser-Beamsplitter R405/488/532/635, Semrock Quad-Notch Filter 405/488/532/635, Semrock
Two-channel detection	Optosplit II (Crain) with Beamsplitter T 635 LPXR, Semrock
Emission filters	BrightLine HC 593/40, Semrock 700/75 ET, Chroma
Camera	iXon ultra DU-897U-CSO-BV, Andor

Table S8. Customized two-color *d*STORM microscope specifications.

parameter	Zeiss LSM 980 Airyscan 2	Zeiss Observer Z.1, Carl Zeiss AG
objective	Plan-Apochromat 20x/0.8 M27 objective	Alpha Plan-Apochromat 63x NA 1.46 Oil Korr, 420780-9970
detector/camera	GaAsP-PMT 747V detector gain, offset, digital gain 1.0	EMCCD Camera EM-Gain: 100, 17.7 photoelectrons per A/D count
pixels per FoV	2658*2658	170*170
Z-stacks	44 slices	-
voxels/pixel size	x,y = 74 nm & z=350 nm	x,y =103 nm
laser excitation	488 nm, 561 nm & 639 nm	532 nm, 639 nm 1-5 kW cm2
channels	sequential Ch1: 420-480nm/495-550nm for 488 nm Ch2: 300-720nm Ch3: 300-720nm	sequential Ch1: 663-738 nm Ch2: 573-613 nm
acquisition	speed: 0.37 µs per pixel bidirectional scanning pinhole: 11.14 (Ch1)/10.50(Ch2) /9.9(Ch3) Airy units	20000 fr 7 ms (Ch1)/13 ms (Ch 2) exposure time
image processing	Zen blue 3.3 (Carl Zeiss AG) a) tiling & stitching 4 times 1*9, 3*3 or 5*2 tiling, fuse tiles, minimal overlap 5%, maximal shift 10% b) Airyscan processing 3D processing, Auto Filer, strength: standard	ThunderSTORM: Image filtering: Wavelet filter(B-spline), order: 3, scale: 2.0; Approximate localization of molecules: Local maximum, peak intensity threshold: x*std(Wave.F1) (x= 1.25-6), 8-neighborhood. Sub-pixel localizations of molecules: Integrated gaussian PSF, fitting radius [px]: 3, weighted least squares, initial sigma [px]: 1.6. Drift correction was performed with gold nanorods as fiducial markers, when visible in the field of view. Filters: 1 nm < uncertainty < 30 nm, 5 < intensity < 2500 photons

Table S9. Acquisition parameters and image processing details. Abbreviations: n/a: not applicable.

Supplementary Figure 1-3

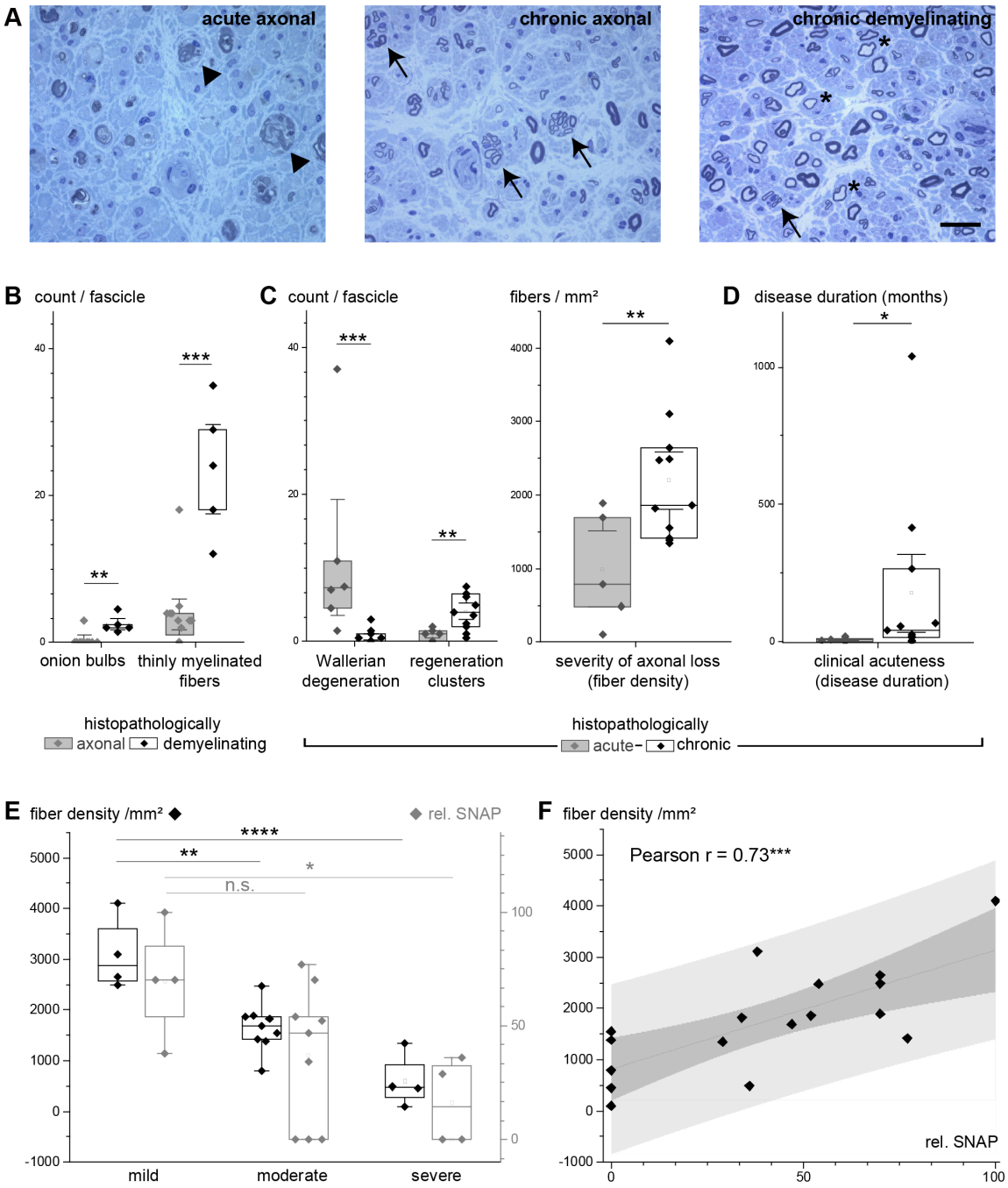

Fig. S1. Histopathological assessment of cross-sectional sensory nerve biopsies and validation. (A) Sensory nerve semithin cross sections with toluidine blue staining in acute axonal neuropathy, chronic axonal neuropathy and demyelinating neuropathy (left to right) show axonal loss with actively degeneration fibers (arrowheads, left) in acute axonal neuropathy, clusters of regenerating fibers in chronic axonal and demyelinating neuropathy (arrows) and thinly myelinated fibers in demyelinating neuropathy (asterisks). Scale bar = 20µm. (B) Histopathological classification by type of disease was validated by comparing the counts per fascicle (y-axis) of onion bulbs and thinly myelinated fibers (x-axis) between biopsies rated as axonal (gray) and demyelinating (black/white, see legend) using Mann-Whitney test. (C) Histopathological classification by acuteness was validated by comparing the counts / fascicle (left graph, y-axis) of Wallerian degeneration figures and regeneration clusters (left graph, x-axis) between biopsies rated as acute (gray) and chronic (black/white, see legend). Fiber density /mm^2 as an indicator of severity of axonal loss (right graph, y-axis) was significantly reduced in acute vs. chronic neuropathy (Student's t test). (D) Histopathological classification was clinically validated by comparing the clinical disease duration in acute vs. chronic neuropathy using Mann-Whitney test. (E-F) Histopathologic classification by severity was validated by nerve conduction studies data (exact values see Supplemental Table 3). (E) Fiber density /mm^2 (left y-axis, black) and relative SNAP in percent of the age-adjusted lower limit of normal (right y-axis, gray) significantly differ according to the severity of axonal loss, assessed by one-way ANOVA with Bonferroni adjustment (fiber density) and Welch one way ANOVA with Dunnett's T3 multiple comparison test (SNAP). (F) Relative SNAP (x-axis) correlated positively to the fiber density (y-axis) using Pearson's correlation coefficient. Significance level: * $p < 0.05$. ** $p < 0.01$, *** $p < 0.001$, **** $p < 0.0001$. Abbreviations: n.s. = not significant, SNAP = sensory nerve action potential.

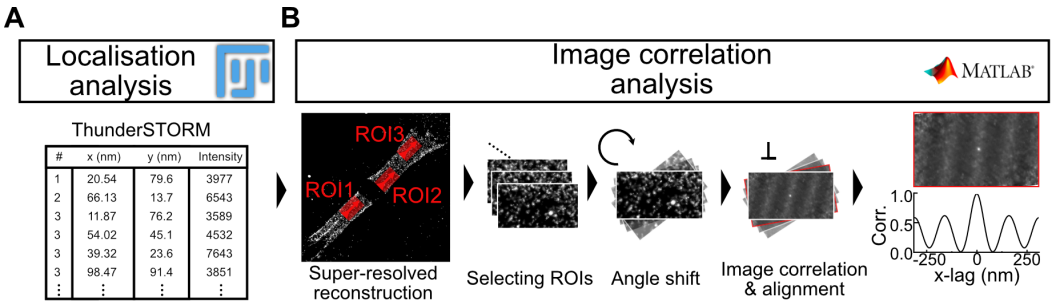

Fig. S2. Image reconstruction and analysis workflow. (A) The ThunderSTORM localisation analysis of the SMLM image sequences provides a list of molecule positions. Based on this list, a super-resolved image of ultrastructural organization of the protein of interest at the node of Ranvier is reconstructed. (B) The Image correlation analysis is performed with a custom MatLab tool which allows to select regions of interest in the super-resolved image. The ROIs are rotated in steps before image auto-correlation to align the pattern perpendicular to the horizontal axis.

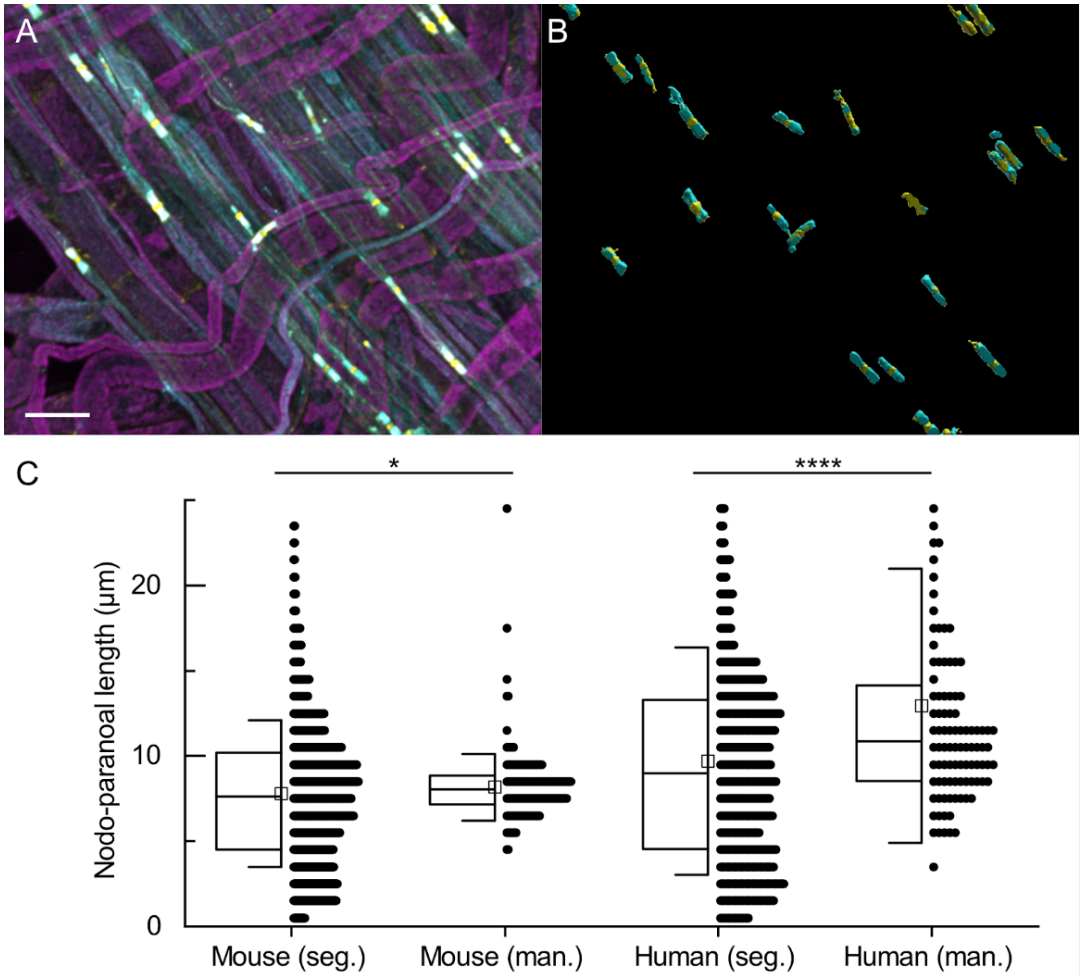

Fig. S3. Assessment of nodo-paranodal length by Imaris segmentation vs. manual FIJI-based routine. (A-B) Murine ischiadic nerve teased fiber preparations with triple-labeling (MBP in magenta, pan-neurofascin in yellow and Caspr-1 in cyan) were segmented using Imaris to identify single nodes of Ranvier. Scale bar = 20 µm. (C) Nodo-paranodal length calculated from Imaris ellipsoid axes (seg.) and manually by ROI definition using FIJI (man.) are compared in murine and human samples. In both, statistically significant differences between automated and manual analysis could be detected (Man-Whitney test: $p = 0.02$, $p < 0.0001$), thus arguing against accuracy of automated measurement. Significance level: * $p < 0.05$. ** $p < 0.01$, *** $p < 0.001$, **** $p < 0.0001$.

Supplementary Movies

Supplementary Movie M1: Assessment of nodo-paranodal parameters based on multicolor large field of view fluorescence imaging. Human sural nerve teased fiber preparations with triple-labeling (MBP in magenta, pan-neurofascin in yellow and Caspr-1 in cyan) were imaged to asses the nodo-paranodal length, paranodal diameter and nodeal gap as indicated in the video. Scale bar = 100 µm.

Supplementary Bibliography

1. Michael P. Collins, P. James B. Dyck, Gary S. Gronseth, Loïc Guillevin, Robert D. M. Hadden, Dieter Heuss, Jean-Marc Léger, N.C. Notermans, John D. Pollard, Gérard Said, Gen Sobue, A.F.J.E. Vrancken, and John T. Kissel. Peripheral nerve society guideline* on the classification, diagnosis, investigation, and immunosuppressive therapy of non-systemic vasculitic neuropathy: executive summary. 15(3):176–184. ISSN 10859489. doi: 10.1111/j.1529-8027.2010.00281.x.
2. Peter Y. K. Van den Bergh, Pieter A. Doorn, Robert D. M. Hadden, Bert Avau, Patrik Vankrunkelsven, Jeffrey A. Allen, Shahram Attarian, Patricia H. Blomkwist-Markens, David R. Cornblath, Filip Eftimov, H. Stephan Goedee, Thomas Harbo, Satoshi Kuwabara, Richard A. Lewis, Michael P. Lunn, Eduardo Nobile-Orazio, Luis Querol, Yusuf A. Rajabally, Claudia Sommer, and Haluk A. Topaloglu. European academy of neurology/peripheral nerve society guideline on diagnosis and treatment of chronic inflammatory demyelinating polyradiculoneuropathy: Report of a joint task force—second revision. 26(3):242–268. ISSN 1085-9489, 1529-8027. doi: 10.1111/jns.12455.
3. Angela Dispenzieri. POEMS syndrome: 2017 update on diagnosis, risk stratification, and management: DISPENZIERI. 92(8):814–829. ISSN 03618609. doi: 10.1002/ajh.24802.